T (K)	a (Å)	b (Å)	c (Å)	V (Å^3)	wR_p
293	6.21108(3)	6.21108(3)	7.36070(4)	283.958(3)	0.089
280	6.20331(5)	6.20331(5)	7.34648(6)	282.701(4)	0.097
260	6.19934(4)	6.19934(4)	7.33636(6)	281.950(4)	0.083
245	6.19578(5)	6.19578(5)	7.33129(7)	281.432(4)	0.074
240	6.19415(5)	6.19415(5)	7.32956(7)	281.217(4)	0.085
235	8.71953(13)	7.35130(9)	8.75930(13)	561.686(12)	0.074
230	8.70298(12)	7.36344(8)	8.75621(12)	561.139(10)	0.070
220	8.67820(14)	7.37495(9)	8.75079(14)	560.063(11)	0.087
200	8.64169(14)	7.39067(9)	8.73969(14)	558.185(10)	0.079
180	8.61319(14)	7.40098(9)	8.72927(14)	556.457(11)	0.082
160	8.58947(15)	7.40814(9)	8.71948(15)	554.837(11)	0.078
140	8.56829(15)	7.41281(10)	8.71018(15)	553.228(11)	0.074
120	8.54919(12)	7.41814(7)	8.70142(12)	551.836(9)	0.092
100	8.53315(5)	7.42110(3)	8.69385(5)	550.541(4)	0.095
80	8.52053(19)	7.42222(12)	8.68620(20)	549.327(15)	0.090

Table 5.7 Unit cell parameters obtained during the low-temperature X-ray powder diffraction experiment conducted on TlN_3.

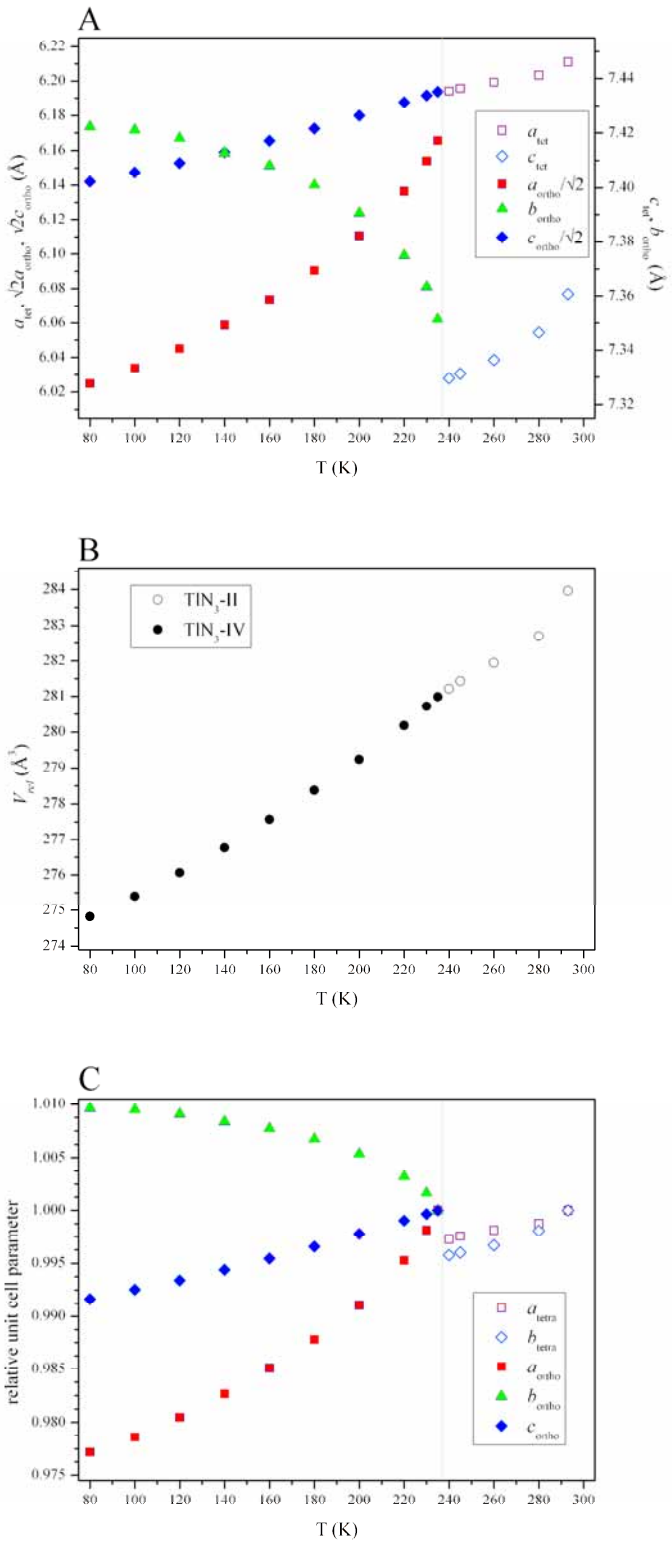

Figure 5.34 (a) Response of the unit cell parameters (*a*, *b* and *c*) to cooling presented alongside $a_{ortho}/\sqrt{2}$ and $c_{ortho}/\sqrt{2}$ to facilitate comparison with the tetragonal cell; (b) the relative volume contraction upon cooling; and, (c) the relative unit cell contraction/expansion throughout the experiment.

The relative contraction or expansion of the unit cell parameters is highlighted in Figure 5.34(c). It should be noted that the unit cell parameters have been normalised to their values at the maximum temperature at which each form has been studied (i.e. 235 K for form IV and 293 K form TlN_3-II). This clearly shows the anomalous expansion of the orthorhombic *b*-axis (corresponding to the *c*-axis in the indexing put forward by Mauer *et al.* [54]), which led previous authors to suggest a transition mechanism involving the 'rotation of one set of the N_3 groups out of the (001) plane' [*sic*].[55] Comparison of the structure of TlN_3-IV at 235 K with the tetragonal form at 240 K (see Figure 5.35), however, shows that there is very little re-arrangement required over this transition, a fact that is reflected in the rapid nature of the transition and the very small volume contraction reported by previous authors.[54, 56] This is in direct contrast to the II → III at 0.7 GPa which does involve an out-of-plane rotation of half the azide units. One would therefore expect a similar transition mechanism to occur upon compression of the low-temperature form IV into the high-pressure regime of form III.

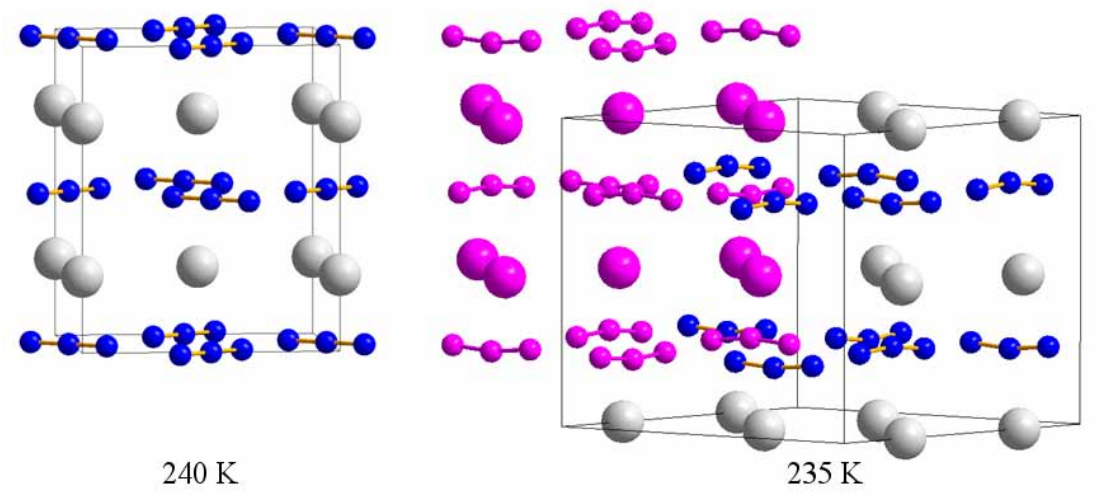

Figure 5.35 The crystal structures determined for TlN_3-II (at 240 K) and TlN_3-IV (at 235 K). In order to facilitate comparison between the related structures, the original tetragonal unit cell has been highlighted in pink in the orthorhombic structure. The deviation from linearity that is observed for the anions in TlN_3-IV may also be seen in the 235 K structure.

The orthorhombic distortion over the II → IV transition is, however, accompanied by a slight displacement of the Tl atoms resulting in a wave-like distribution. This feature becomes more pronounced upon cooling (4° at 235 K to 8° at 80 K), mirroring the behaviour observed throughout compression of TlN_3-III. This results in the appearance of small peaks in the diffraction pattern, which can only be modelled by the displacement of the thallium atoms away from (0.75, *y*, *z*), as depicted in Figure 5.36. It should also be noted that neither of the azide groups are linear (despite the restraints applied to these groups), although it has

been difficult to refine the positions of the nitrogen atoms due to the minimal contribution they make to the total X-ray scattering in this case.

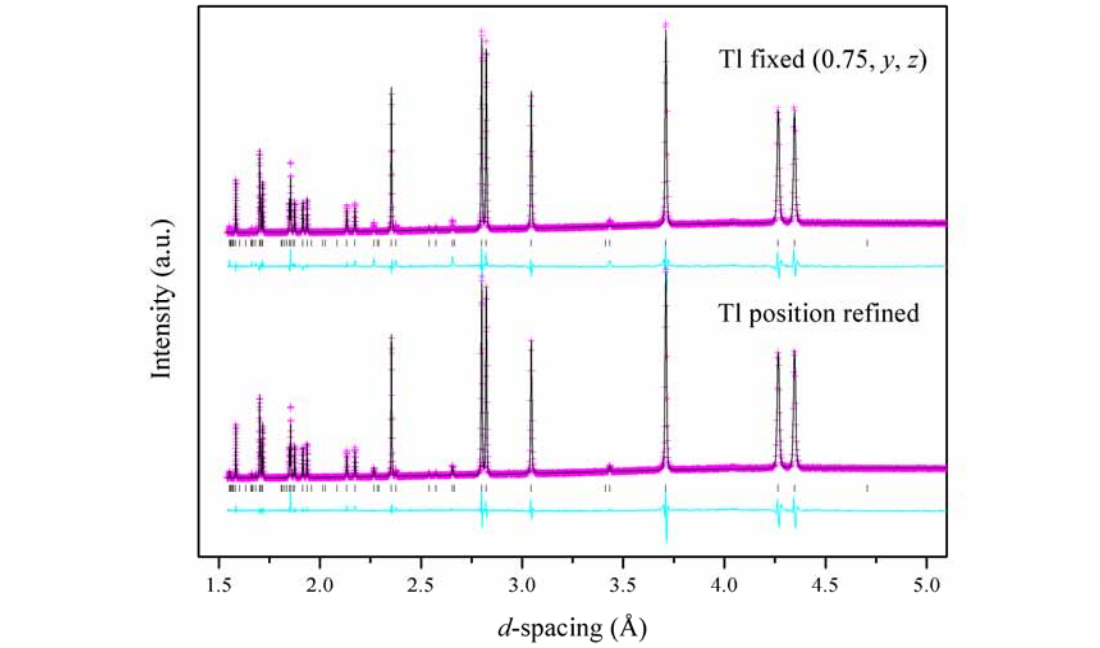

Figure 5.36 Comparison of the Rietveld refinements in which the thallium positions are refined and are fixed (bottom and top, respectively). In both cases, the observed intensities (I_{obs}) are plotted in pink, the calculated pattern (I_{calc}) in black and the difference curve ($I_{obs} - I_{calc}$) is shown in cyan. It should be noted that the top refinement (Tl fixed) does not accurately re-create the observed intensities at d = 2.25, 2.65 and 3.45 Å, corresponding to the (023), (221) and (021) reflections, respectively.

The exact reason for the anomalous expansion of the *b*-axis is still to be determined – one would expect a planar structure such as this to exhibit a preferential contraction of the interplanar distance, rather than expansion along it. Moreover, the observation that a single crystal did not survive the low-temperature transition is surprising, especially given the structural similarities between the two forms in the temperature range immediately surrounding the transition point. This perhaps indicates a more complex transition mechanism involving the azide groups. It would therefore be extremely desirable to conduct an analogous low-temperature neutron diffraction study in order to accurately determine the nitrogen positions. This would also allow an accurate assessment of the linearity (and symmetry) of the azide groups, thus providing an important insight into the interactions between the anions and the thallium cations.

Ambient-Pressure, High-Temperature Study

In order to provide complementary experimental evidence of the II → I transition at high temperatures, X-ray powder diffraction data were collected upon warming a freshly prepared sample of TlN_3 between 320 and 575 K. The diffraction patterns collected over the phase transition are presented in Figure 5.37, in which two important features are highlighted. First, the abrupt loss in intensity of the (004) and (114) peaks at d = 1.87 and 1.72 Å, respectively, upon warming from 550 to 560 K; secondly, the appearance of a new peak at d = 2.76 Å in the pattern collected at 570 K, becoming more prominent in the 575 K pattern. The latter feature is perhaps indicative of partial sample decomposition; the peak at 2.76 Å coincides with the strongest peak of the cubic high-temperature form of thallium metal ($Im\bar{3}m$) [85, 86], although it should be noted that no other peaks attributable to β-Tl are present in the 575 K pattern. Unfortunately the relatively low signal-to-noise ratio has made the determination of the temperature at which sample decomposition first occurs difficult. It would therefore be advantageous to repeat this study using either longer data collection times, high-resolution X-ray powder diffraction (as in the low-temperature study above) or neutron powder diffraction, thus providing an invaluable insight into the thermal stability of TlN_3.

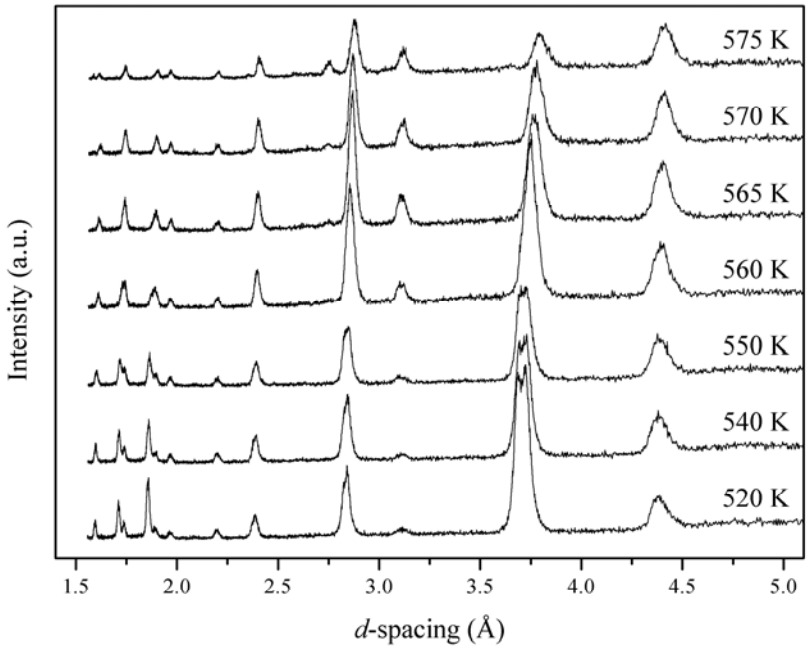

Figure 5.37 X-ray powder diffraction patterns collected for TlN_3 over the II – I phase transition (520 – 575 K).

The reduction in intensity of the (004) and (114) peaks is more likely indicative of a phase transition within the sample. Thus the TlN_3-II → I transition has been observed to occur between 550 and 560 K, below the previous experimental transition temperature (568 K reported by Müller and Jöbstl [37]) and above that observed in Molecular Dynamics (MD) simulations (530 K).[53] Supporting evidence for the phase transition occurring between 550 and 560 K can be found by plotting the unit cell parameters determined by Le Bail refinement of each of the diffraction patterns. In addition, these data have been corroborated manually by fitting Pseudo-Voigt functions to (002), (004), (110) and (220) peaks. A summary of all the data can be found in Table 5.8 and Figure 5.38. It should be noted that in this case, the phase transition has simply been modelled by a marked lengthening of the unit cell axes (primarily the *c*-axis), while maintaining the space group symmetry. This is in accordance with the procedure followed by Liu *et al.* who describe the high-temperature cubic form as a distortion of the original tetragonal cell.[53] The unit cell axes are shown in Figure 5.38 to undergo a thermal expansion of < 1.0% in the temperature range 320 – 550 K; in the high-temperature form, however, the relative expansion between 550 and 575 K *ca* 1.5 times this.

T (K)	a, b (Å)	c (Å)	V (Å^3)	R_p
320	6.1981(7)	7.3810(9)	283.55(9)	0.103
340	6.2062(6)	7.3571(6)	283.38(6)	0.137
360	6.2073(7)	7.3649(6)	283.77(7)	0.187
380	6.2049(7)	7.3723(5)	283.84(6)	0.183
400	6.2076(6)	7.3764(4)	284.25(5)	0.117
420	6.2030(7)	7.3779(4)	283.88(6)	0.195
440	6.2048(7)	7.3837(4)	284.26(6)	0.138
460	6.2066(7)	7.3906(4)	284.70(6)	0.176
480	6.2056(8)	7.4032(9)	285.10(7)	0.243
500	6.2023(6)	7.4071(5)	284.94(6)	0.252
520	6.2087(6)	7.4126(4)	285.74(6)	0.153
540	6.2089(6)	7.4247(4)	286.22(5)	0.135
550	6.2083(5)	7.4378(5)	286.67(5)	0.157
560	6.2094(5)	7.4922(5)	288.87(4)	0.163
565	6.2139(5)	7.5313(7)	290.81(5)	0.196
570	6.2135(5)	7.5569(8)	291.75(5)	0.260
575	6.2220(8)	7.5812(13)	293.50(8)	0.202

Table 5.8 Unit cell parameters (a, c, V) determined by Le Bail refinement of the X-ray powder diffraction patterns. R_p factors are reported in this case since it has not been possible to carry out full-profile refinements of the X-ray powder diffraction patterns collected, resulting in larger than desirable values of χ^2 and hence wR_p.

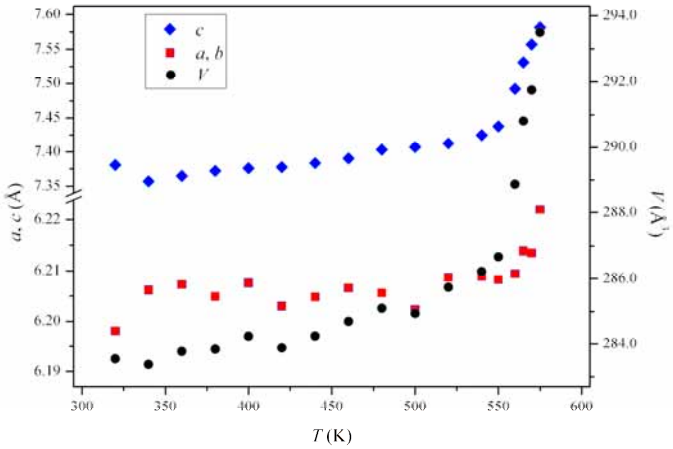

Figure 5.38 Expansion of the unit cell parameters (a, c, V) with temperature, as determined by Le Bail refinement.

A further interesting aspect of this variable temperature study, which may have significant implications for the treatment of the disorder model proposed for this system, is the reduction of the intensities of the (002) and (004) peaks 90 K below the proposed phase transition. Again Pseudo-Voigt functions have been fitted to each peak and their intensities have been normalised to (a) the intensity of each peak at 320 K, and (b) the (112) peak at each temperature, the intensity of which was observed not to vary considerably up to 550 K. A plot of the normalised intensities versus temperature can be found in Figure 5.39, alongside a representation of the diminishing intensity of the (004) peak. It should be noted that the intensity of each peak does not vary significantly upon warming to 460 K, indicating the temperature effect on the diffraction intensities to be negligible. The selective reduction in intensity of some of the Bragg peaks between 460 and 550 K would rather seem to suggest a degree of internal disorder, preceding the phase transition. The exact nature of this disorder is still to be fully explored experimentally. However, the observation that the (002) peak (corresponding to the *hkl* plane, in which half the azide anions are situated) and the (004) peak (affected solely by thallium atoms) are *both* diminished would indicate that the disorder mechanism involves motion of both the anions and the cations.

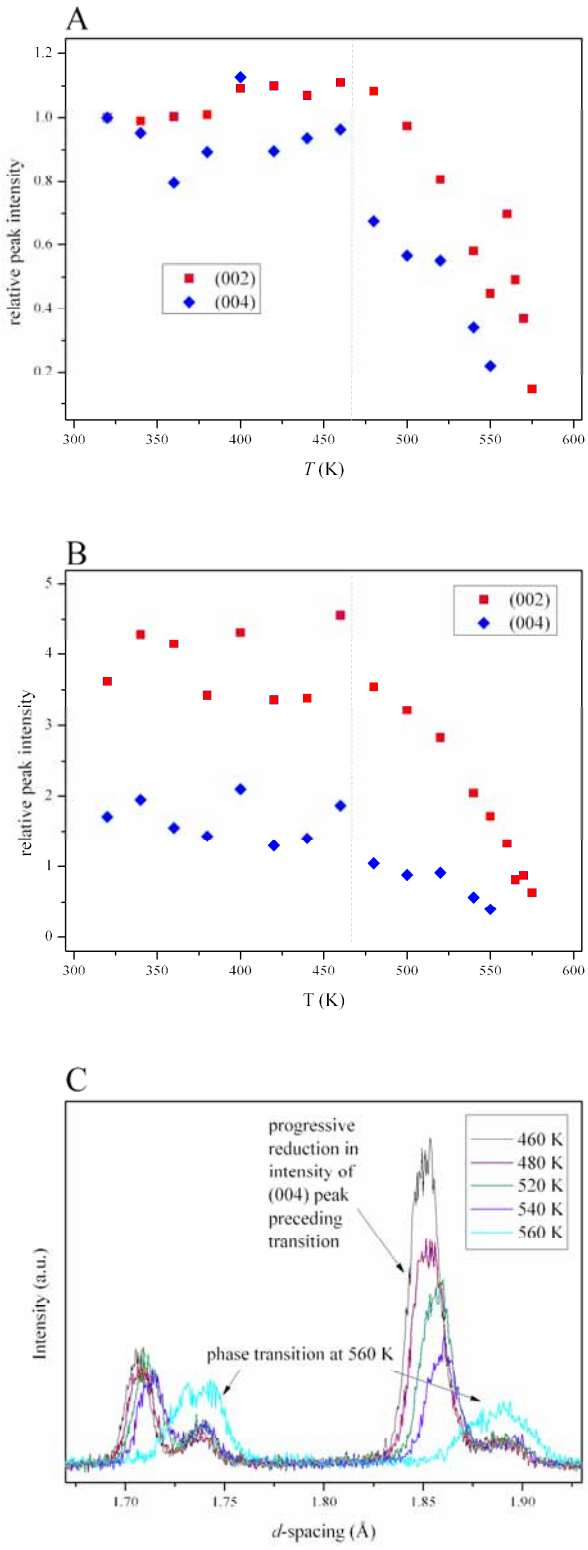

Figure 5.39 Plots of (a) the intensity of the (002) and (004) peaks with respect to their intensities in the 320 K pattern, and (b) the intensity relative to the (112) peak. It should be noted that the (004) peak cannot be distinguished from the background above 550 K. The dashed line represents the temperature at which the disorder is proposed to commence. The reduction in intensity of the (004) on warming is shown in (c) alongside the pattern collected at 560 K, after the phase transition.

Finally in this study, the recoverability of the high-temperature form I was explored by cooling the sample back to 300 K over *ca* 12 hrs. A comparison of the diffraction pattern collected for the recovered phase with those collected at 575 and 320 K is presented in Figure 5.40. In order to ensure that complete transformation to this phase had occurred, additional data collections were performed after 12 and 24 hrs. No significant changes in peak position or intensity were observed over this timeframe. Visual inspection of the diffraction patterns suggests that the recovered pattern shares similarities with both the pattern collected at 320 K (form I) and that collected at 575 K (form II), indicating the presence of either a mixed phase, or perhaps a novel polymorph obtained upon cooling. Unfortunately the low resolution of the diffraction pattern and the unsatisfactory signal-to-noise ratio has meant that it has not been possible to exclude the possibility of sample decomposition at elevated temperatures. Diffraction peaks attributable to the hexagonal ambient temperature form of thallium metal (at d = 2.62, 2.74 and 2.99 Å) are either overlapped by TlN_3 sample peaks or may not be suitably distinguished from the background. High-resolution X-ray powder diffraction on the recovered sample is currently being investigated, with a view to providing conclusive evidence for the presence (or otherwise) of Tl(s) and to allow indexing of the remaining TlN_3 sample.

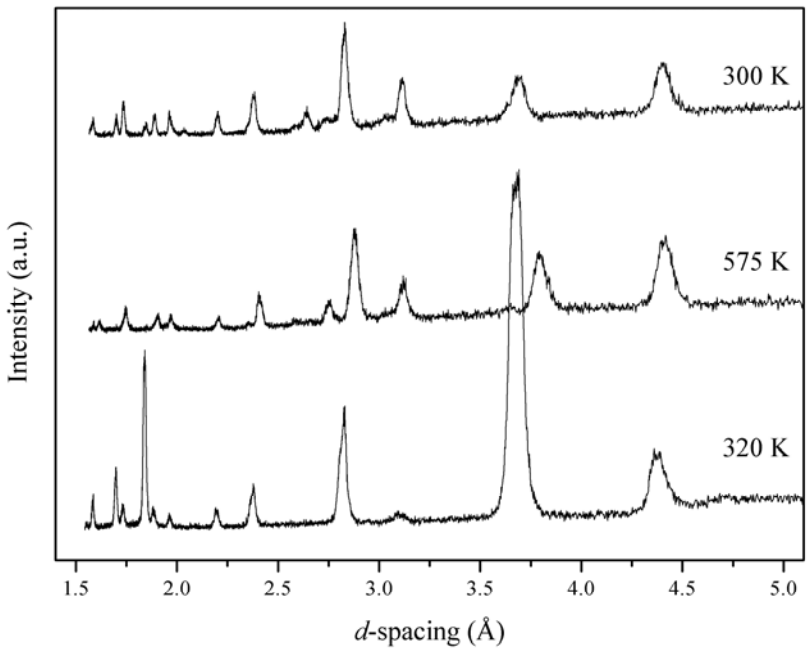

Figure 5.40 Comparison of the X-ray powder diffraction patterns collected at 320 and 575 K, along with the pattern collected for the recovered sample (at 300 K).

Summary: TlN_3

The high-pressure, ambient-temperature behaviour of thallium azide has been investigated by neutron powder diffraction. TlN_3-II has been shown to remain stable upon compression to a maximum of 0.74 GPa: in this region compression is surprisingly isotropic and is not accompanied by any significant rotation of the azide anions. Structure solution of TlN_3-III (*Immm*) has shown that a dramatic re-arrangement of the anions occurs over the II → III transition (at 0.76 GPa). This high-pressure form III has been shown to remain stable up to the maximum pressure studied (6.98 GPa) although the appearance of a new peak in the neutron powder diffraction patterns collected above 3.69 GPa may be indicative of a subtle phase transition at this pressure.

In addition to the high-pressure form III, the structure of the low-temperature form-IV (*Cmcm*) has been determined for the first time. The cell-doubling associated with the phase transition is in accordance with previous experimental data [54, 55], but no significant re-organisation of the anions is observed, on the basis of our X-ray powder diffraction data. Moreover the thallium cations are distributed in a wave-like fashion, similar to TlN_3-III, but in contrast the azide anions deviate significantly from linearity. Neutron powder diffraction experiments are planned to confirm this structural model.

Finally the high-temperature phase transition (II → I) has been shown to occur between 550 and 560 K. This transition temperature is lower than that observed in the only previous experimental report (568 K) [37], although it is possible that Müller and Jöbstl were actually observing partial sample decomposition, which we observe to commence ~ 570 K. The variable temperature X-ray powder diffraction study presented herein has provided experimental evidence to complement the MD simulations reported by Liu *et al.* [53] Both studies indicate that a significant degree of disorder occurs preceding the II → I transition, although neutron diffraction experiments are advised to obtain an accurate description of the atomic thermal motions in this temperature regime.

5.6 Summary and Conclusions

Given the relative structural simplicity of the inorganic azides, particularly the compounds studied in this chapter, the polymorphism they display is remarkable. The fact that each of NaN_3, CsN_3 and TlN_3 have been found to adopt *at least* three different crystal structures at extreme conditions highlights the dramatic effect that even modest pressure (*ca* 0.5 GPa) has on the relative energies of different crystalline systems. These results will therefore be invaluable to solid state chemists and physicists who seek to create accurate computational

models for these systems. Furthermore, it is hoped that the structural characterisation of these materials under a range of pressure and temperature conditions will provide an insight into their energetic performance and may facilitate the rationalisation of their respective sensitivities. The table of structural information for these three compounds has been updated to reflect the advances made in this study. This is presented in Table 5.9 below.

The α-form of sodium azide has been shown to remain stable during compression at ambient temperature. However, the combined effects of temperature and pressure were sufficient to prompt a phase transition to a tetragonal γ-form. Interestingly, this form is isostructural with CsN_3 and RbN_3 and, in this case, one may therefore consider pressure to be acting to force sodium to behave like a larger group 1 element, adopting a larger co-ordination number. Furthermore, the considerable structural re-arrangement required for a $\gamma \rightarrow \alpha$ transition results in significant kinetic barrier to this transition, which is reflected in the observed hysteresis behaviour. Upon complete decompression to ambient pressure, a sample of the α-form was recovered, although considerable crystallographic strain was evident in the neutron powder diffraction pattern. This dramatic reduction in sample quality may have implications for sensitivity, particularly if further phase transitions were to occur at even higher pressures and/or temperatures during detonation events.

The ambient-pressure, high-pressure polymorphism of CsN_3 has been found to be unexpectedly rich – three high-pressure forms have been identified, although only one of these has been structurally characterised. X-ray powder diffraction studies of these high-pressure forms, meanwhile, have been hampered by sample decomposition in the high-energy synchrotron beam. This apparent photolysis at pressure, however, may prove to be an even more exciting prospect since this may present a relatively facile route to highly desirable polynitrogen species. It will therefore be essential to conduct rigorous studies not only to determine the structure of the parent CsN_3 species at extreme conditions but also to characterise the photolysis products and their recoverability.

Finally, the high-pressure and the low-temperature structures (forms III and IV, respectively) of thallium azide have been determined. While the low-temperature phase transition has been observed to involve a simple orthorhombic distortion of the tetragonal TlN_3-II, the $II \rightarrow III$ transition involves a more holistic rearrangement. In addition to these new forms, the high-temperature form I was investigated by X-ray powder diffraction. Although the quality of the diffraction data was not sufficient to allow Rietveld refinement of the structure during warming, striking evidence of a phase transition was observed between 550 and 560 K. Furthermore, it is suggested that the reduction in intensity of select peaks in the diffraction

Polymorph	Space Group	*a* (Å)	*b* (Å)	*c* (Å)	*α* (°)	*β* (°)	*γ* (°)	Atomic positions?	*P*/*T* conditions	Ref.
α-NaN_3	*C*2/*m*	6.1654(5)	3.6350(3)	5.2634(6)	90	107.543(5)	90	Yes	Ambient *P*; *T* < 292 K *P* > 0.07 GPa; Ambient *T*	[25],[39]
β-NaN_3	$R\bar{3}m$	3.646(2)	3.646(2)	15.213(5)	90	90	120	Yes	Ambient *P*; *T* > 292 K	[8]
γ-NaN_3	***I4/mcm***	**5.6114(3)**	**5.6114(3)**	**6.0418(4)**	**90**	**90**	**90**	**Yes**	***P* > 3.12 GPa; *T* > 393 K**	**this study**
CsN_3-I	$Pm\bar{3}m$	4.53(1)	4.53(1)	4.53(1)	90	90	90	No	Ambient *P*; *T* > 424 K	[37]
CsN_3-II	*I*4/*mcm*	6.5412(4)	6.5412(4)	8.0908(5)	90	90	90	Yes	Ambient *P*; *T* < 424 K	[44]
CsN_3-III	***P*2$_1$/*c***	**9.8858(8)**	**6.1327(7)**	**6.2119(10)**	**90**	**120.054(8)**	**90**	**Yes**	**0.54 GPa < *P* < 3.6 GPa; Ambient *T***	**this study**
CsN_3-IV	-	-	-	-	-	-	-	-	**3.6 GPa < *P* < 4.8 GPa; Ambient *T***	**this study**
CsN_3-V	-	-	-	-	-	-	-	-	***P* > 4.8 GPa; Ambient *T***	**this study**
TlN_3-I	$Pm\bar{3}m$	-	-	-	90	90	90	No	Ambient *P*; *T* > 568 K	[37]
TlN_3-II	*I*4/*mcm*	6.208(1)	6.208(1)	7.355(2)	90	90	90	Yes	Ambient *P*; 248 K < *T* < 568 K	[44]
TlN_3-III	***Immm***	**5.8274(6)**	**5.4141(3)**	**8.4670(7)**	**90**	**90**	**90**	**Yes**	***P* > 0.76 GPa; Ambient *T***	**this study**
TlN_3-IV	***Cmcm***	**8.71953(13)**	**7.35130(9)**	**8.75930(13)**	**90**	**90**	**90**	**Yes**	**Ambient *P*; *T* < 235 K**	**this study**

Table 5.9 Structural information for all polymorphs of sodium azide, caesium azide and thallium azide, including the structural data determined in this study (emboldened).

pattern commencing at 460 K is indicative of the initiation of a disorder model although planned neutron powder diffraction studies are expected to elucidate this behaviour.

5.7 Suggestions for Further Work

The X-ray powder diffraction experiments conducted in this work, although instructive, have been hampered by the dominance of the scattering from the heavy metals (Cs and Tl). It has therefore been proposed that variable temperature neutron powder diffraction studies be conducted. This will not only allow the definitive structure solution of the low-temperature form of TlN_3 by the refinement of the nitrogen positions but will also facilitate the thorough examination of the high-temperature behaviour of TlN_3 and CsN_3. It is hoped that it will be possible to characterise any disorder preceding the tetragonal → cubic (II → I) phase transition, as well as obtaining structural data on the high-temperature forms of each compound.

Furthermore, it would be worthwhile re-examining the high-pressure behaviour of TlN_3, in order to determine whether the presence of the additional peak above 3.69 GPa is actually evidence of a further phase transition. Unfortunately, it was not possible to explore the decompression behaviour of TlN_3 and this should therefore be investigated at the earliest possible opportunity. This will provide important information on the recoverability of the high-pressure phase(s) *and* the effect these transitions have on sample quality.

As has been stated above, the opportunity of obtaining polynitrogen species by the photolysis of simple azides at elevated pressures is particularly exciting. The initial focus of these experiments should certainly be the identification and characterisation of the photolysis products, as well as the conditions necessary for photolysis to occur. It is also recommended that such studies should not be limited to CsN_3. While X-ray powder diffraction has been successful in these initial studies, a range of analytical techniques should be explored in future. It is expected that vibrational spectroscopy may be particularly sensitive to the formation of 'non-molecular' nitrogen species, as it will be relatively straightforward to identify any spectral bands that cannot be attributed to the azide anions. Should this method be successful, the focus of these studies will naturally shift to the recovery of these species to ambient conditions.

Finally, it would also be interesting to examine the anomalous compression behaviour of sodium azide at very low pressures. While it is reasonable to suggest that the lengthening of the *b*-axis between 0.0 and 0.5 GPa simply arises due to a particularly anisotropic compression mechanism, such behaviour may also be indicative of a subtle structural

modification. In order to characterise this compression behaviour fully, a gas cell experiment using high-resolution neutron powder diffraction is advised. The gas cell is recommended since it allows the compression to be performed in small, and exact, pressure increments. Meanwhile, the increased resolution of a beamline such as POLARIS (ISIS) would highlight any structural nuances that may not have been detected during the present work.

5.8 References

1. J. Giles, *Nature*, 2004, **427**, 580.
2. M.H.V. Huynh, M.A. Hiskey, T.J. Meyer, and M. Wetzler, *Proc. Nat. Acad. Sci. USA*, 2006, **103**, 5409.
3. E.W. Sidebottom, *US Patent Appl. 05/375,654*, 1973
4. S.M. Peiris and T.P. Russell, *J. Phys. Chem. A*, 2003, **107**, 944.
5. M.I. Eremets, M.Y. Popov, I.A. Trojan, V.N. Denisov, R. Boehler, and R.J. Hemley, *J. Chem. Phys.*, 2004, **120**, 10618.
6. U. Müller, *Strukturchemie der Azide*, in *Structure and Bonding, Inorganic Chemistry, Vol. 14*, 1973, Springer, Berlin/Heidelberg.
7. I.C. Tornieporth-Oetting and T.M. Klapötke, *Angew. Chem. Int. Ed.*, 1995, **34**, 511.
8. G.E. Pringle and D.E. Noakes, *Acta Cryst.*, 1968, **B24**, 262.
9. I.D. Campbell and C.K. Coogan, *J. Chem. Phys.*, 1966, **44**, 2075.
10. M. Cartwright and J. Wilkinson, *Propellants, Explos., Pyrotech.*, 2010, **35**, 326.
11. A.B. Gordienko, Y.N. Zhuravlev, and A.S. Poplavnoi, *Phys. Status Solidi B*, 1996, **198**, 707.
12. A.B. Gordienko and A.S. Poplavnoi, *Russ. Phys. J.*, 2004, **47**, 1056.
13. W. Zhu, J. Xiao, and H. Xiao, *J. Phys. Chem. B*, 2006, **110**, 9856.
14. W. Zhu and H. Xiao, *J. Phys. Chem. B*, 2006, **110**, 18196.
15. W. Zhu and H. Xiao, *J. Comput. Chem.*, 2008, **29**, 176.
16. V. Lisitsyn, Y. Zhuravlev, V. Oleshko, D. Fedorov, and V. Tsipilev, *High Energy Chem.*, 2006, **40**, 218.
17. G.J. Piermarini, *J. Res. Natl. Inst. Stand. Technol.*, 2001, **106**, 889.
18. C.E. Weir, S. Block, and G.J. Piermarini, *J. Chem. Phys.*, 1970, **53**, 4265.
19. S.B. Hendricks and L. Pauling, *J Am. Chem. Soc.*, 1925, **47**, 2904.
20. J.I. Bryant, *J. Chem. Phys.*, 1964, **40**, 3195.
21. C.S. Choi and E. Prince, *J. Chem. Phys.*, 1976, **64**, 4510.
22. E.D. Stevens and H. Hope, *Acta Cryst.*, 1977, **A33**, 723.
23. Z. Iqbal, *J. Chem. Phys.*, 1973, **59**, 1769.
24. B.S. Miller and G.J. King, *J. Chem. Phys.*, 1963, **39**, 2779.
25. S.R. Aghdaee and A.I.M. Rae, *Acta Cryst.*, 1984, **B40**, 214.
26. Z. Iqbal, *Advances in Raman Spectroscopy*, 1972, **1**, 188.
27. J.C. Raich and N.S. Gillis, *J. Chem. Phys.*, 1976, **65**, 2088.
28. J.C. Raich and A. Huller, *J. Chem. Phys.*, 1979, **70**, 3669.
29. R.C. Carling and E.F. Westrum Jnr., *J. Chem. Thermodynamics*, 1976, **8**, 565.
30. S. Hirotsu, M. Miyamota, and K. Ema, *J. Phys. C: Solid State Physics*, 1983, **16**, L661.
31. M. Midorikawa, H. Orihara, Y. Ishibashi, T. Minato, and H. Terauchi, *J. Phys. Soc. Jpn*, 1983, **52**, 3833.
32. S. Hirotsu, *J. Phys. C: Solid State Physics*, 1983, **16**, L1103.
33. K.R. Jeffrey, *J. Chem. Phys.*, 1977, **66**, 4677.
34. S.R. Aghdaee and A.I.M. Rae, *J. Chem. Phys.*, 1983, **79**, 4558.
35. T. Kushida and R.W. Terhune, *Phys. Rev. B: Condens. Matter*, 1986, **34**, 5791.
36. G.J. Simonis and C.E. Hathaway, *Phys. Rev. B: Condens. Matter*, 1974, **10**, 4419.

37. H.J. Müller and J.A. Jöbstl, *Z. Kristallogr.*, 1965, **121**, 385.
38. R.S. Bradley, J.D. Grace, and D.C. Munro, *Z. Kristallogr.*, 1964, **120**, 349.
39. C.W. Christoe and Z. Iqbal, *Chem. Phys. Lett.*, 1976, **39**, 511.
40. K. Knorr and W. Depmeier, *High Pressure Res.*, 2000, **17**, 297
41. C.W.F.T. Pistorius and A.J. Campbell White, *High Temperatures - High Pressures*, 1970, **2**, 507.
42. T.C. Waddington, *J. Chem. Soc*, 1959, 2499.
43. A. Fuith, *Phase Transitions*, 1997, **62**, 1
44. U. Müller, *Z. Anorg. Allg. Chem.*, 1972, **392**, 159.
45. J.I. Bryant, *J. Chem. Phys.*, 1966, **45**, 689.
46. C.E. Hathaway and P.A. Temple, *Phys. Rev. B: Condens. Matter*, 1971, **3**, 3497.
47. Z. Iqbal and C.W. Christoe, *J. Chem. Phys.*, 1975, **62**, 3246.
48. C.W.F.T. Pistorius, *J. Chem. Phys.*, 1969, **51**, 2604.
49. P. da R. Andrade, A.D.P. Rao, R.S. Katiyar, and S.P.S. Porto, *Solid State Commun.*, 1973, **12**, 847.
50. M.M. Ossowski, J.R. Hardy, and R.W. Smith, *Phys. Rev. B: Condens. Matter*, 1999, **60**, 15094.
51. O. Reckeweg and A. Simon, *Z. Naturforsch.*, 2003, **58**, 1097.
52. F.J. Owens, *J. Phys. C: Solid State Physics*, 1979, **12**, 2255.
53. J. Liu, C.G. Duan, M.M. Ossowski, W.N. Mei, R.W. Smith, and J.R. Hardy, *Mater. Res. Bull.*, 2001, **36**, 2035.
54. F.A. Mauer, C.R. Hubbard, and T.A. Hahn, *J. Chem. Phys.*, 1973, **59**, 3770.
55. Z. Iqbal and C.W. Christoe, *Chem. Phys. Lett.*, 1974, **29**, 623.
56. C.W.F.T. Pistorius, *J. Chem. Phys.*, 1974, **60**, 3720.
57. C.W. Christoe and Z. Iqbal, *Solid State Commun.*, 1974, **15**, 859.
58. W.G. Marshall and D.J. Francis, *J. Appl. Crystallogr.*, 2002, **35**, 122.
59. A.D. Fortes, PhD Thesis, 2004, Department of Earth Sciences, University College, London, UK.
60. J.M. Besson, R.J. Nelmes, G. Hamel, J.S. Loveday, G. Weill, and S. Hull, *Physica B*, 1992, **180-181**, 907.
61. R. Von Dreele and A.C. Larson, *General Structure Analysis System (GSAS)*, 1986.
62. W.G. Marshall, D.J. Francis, C.J. Barry, O. Kirichek, C.R. Pulham, and M.G. Tucker, *manuscript in preparation*, 2010.
63. L. Merrill and W.A. Bassett, *Rev. Sci. Instrum.*, 1974, **45**, 290.
64. G.J. Piermarini, S. Block, J.D. Barnett, and R.A. Forman, *J. Appl. Phys.*, 1975, **46**, 2774.
65. A.P. Hammersley, S.O. Svensson, M. Hanfland, A.N. Fitch, and D. Hausermann, *High Press. Res.*, 1996, **14**, 235
66. Bruker-AXS, *D8-Advance*, Madison, WI, USA, 2002.
67. Bruker-AXS, *D8-Advance*, Madison, WI, USA, 2010.
68. J. Cosier and A.M. Glazer, *J. Appl. Crystallogr.*, 1986, **19**, 105.
69. Anton-Paar, *TTK-450*, Graz, Austria, 1998.
70. T. Boffa-Ballaran and R.J. Angel, *Eur. J. Mineral.*, 2003, **15**, 241.
71. F. Birch, *Phys. Rev.*, 1947, **71**, 809.
72. R.J. Angel, *EOS-FIT V5.2*, Department of Geological Sciences, Virginia Tech., Blacksburg, VA, USA, 2001.
73. R.J. Angel, *Equations of State*, in *Reviews in Mineralogy and Geochemistry, 41: High-Temperature and High-Pressure Crystal Chemistry*, R.M. Hazen and R.T. Downs, Editors, 2000, Mineralogical Society of America, Washington, D.C., USA.
74. S.A. Medvedev, I.A. Trojan, M.I. Eremets, T. Palasyuk, T.M. Klapötke, and J. Evers, *J. Phys. Condens. Matter*, 2009, **21**, 195404.
75. H. Spetzler, C.G. Sammis, and R.J. O'Connell, *J. Phys. Chem. Solids*, 1972, **33**, 1727.

76. J.L. Feldman, M.J. Mehl, L.L. Boyer, and N.C. Chen, *Phys. Rev. B*, 1988, **37**, 4784.
77. D. Louër and A. Boultif, *Z. Kristallogr. Suppl.*, 2007, **26**, 191.
78. S. Zhang, H. Li, H. Li, S. Zhou, and X. Cao, *J. Phys. Chem. B*, 2007, **111**, 1304.
79. F.C. Tompkins and D.A. Young, *Proc. R. Soc. London, Ser. A*, 1956, **236**, 10.
80. H.A. Papazian, *J. Phys. Chem. Solids*, 1965, **27**, 906.
81. B.H. Krause, *J. Chem. Phys.*, 1963, **39**, 1706.
82. G.J. King, F.F. Carlson, B.S. Miller, and R.C. McMillan, *J. Chem. Phys.*, 1961, **34**, 1499.
83. Accelrys, *Materials Studio*, Sand Diego, CA, USA, 2010.
84. R. Von Dreele, *personal communication*, 2010.
85. H. Lipson and A.R. Stokes, *Nature*, 1941, **148**, 437.
86. E.G. Ponyatovskii and A.I. Zakharov, *Kristallografiya*, 1962, **7**, 461.

Chapter 6

Structural Investigation of a Series of Inorganic Azides

Part 2: NH_4N_3, AgN_3 and $Pb(N_3)_2$

6 Structural Investigation of a Series of Inorganic Azides (Part 2)

6.1 Polymorphism of the 'More Complex' Inorganic Azides

6.1.1 NH_4N_3

The structure of ammonium azide is also based on a modification of the basic CsCl cubic structure although hydrogen bonding plays a dominant role in the distortion. The azide anions are broadly organised into layers, but half of the anions are rotated out of the plane to allow hydrogen bonding between the ammonium ion and the negative termini of the azide ions. This results in half of the anions lying parallel to the *a*-axis (Type I), while the other half lie perpendicular to *a* (Type II), thus allowing a tetrahedral arrangement of azide termini around a single cation (Figure 6.1).

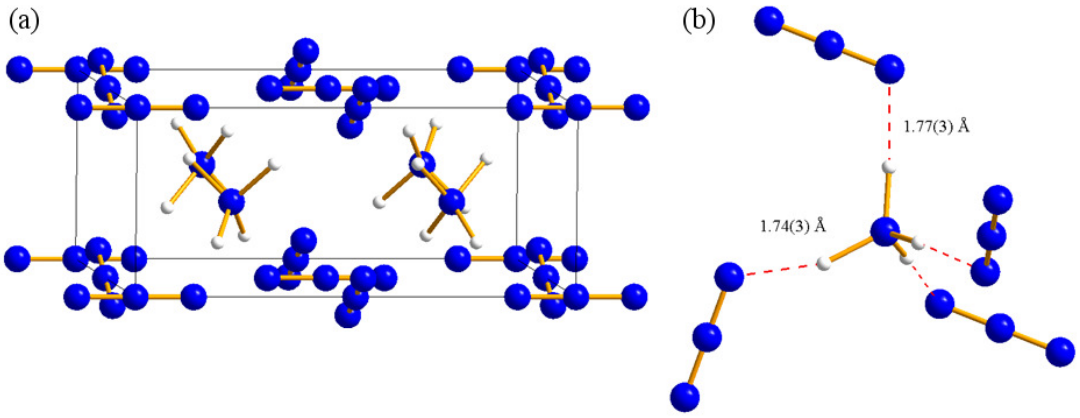

Figure 6.1 (a) Structure of ammonium azide, highlighting the layers of azide anions, in which the anions that are normal to the *a*-axis are rotated out of the *ac*-plane; and, (b) the N-H…N hydrogen bonding interactions.

The space group (*Pmna*) and nitrogen positions were determined in 1936 and from these data it was possible to infer the existence of strong H-bonds and that the ammonium ion adopts a definite orientation at room temperature, which is not spherically averaged.[1] This was subsequently confirmed spectroscopically.[2] A full structural refinement was subsequently performed using single-crystal neutron diffraction.[3] NH_4N_3 has recently been used as a test case for *ab initio* structure solution from X-ray powder diffraction using synchrotron radiation.[4] The authors successfully (re)-determined the structure of this light-atom structure, including hydrogen positions – their structural model was in good agreement with the structure obtained from single-crystal neutron data. Single-crystal X-ray diffraction results published in 2003 were also in accordance with the proposed structure.[5]

Low temperature spectroscopic measurements indicate that no phase transitions occur upon cooling to 68 K [6] and thermal analysis up to the sublimation point (408 K) showed no anomalies indicative of a phase transition to a high-temperature form.[7] No variable pressure studies have ever been reported in the open literature. This study therefore aims to be the first such investigation and uses neutron powder diffraction to characterise the compression behaviour of ND_4N_3 to a maximum pressure of 4.9 GPa.

6.1.2 AgN_3

Silver azide may be regarded as an intermediary between the ionic azides described above and the co-ordinative azides of other heavy metals (such as copper and lead).[8] In common with the ionic azides, the unit cell is based on the CsCl cubic structure and the N_3^- ions are linear and symmetric. In fact, the orthorhombic (*Ibam*) structure adopted at ambient temperature and pressure is in many regards consistent with the tetragonal structure found in CsN_3 and TlN_3, although a lengthening of the crystallographic *b*-axis reduces the symmetry to an orthorhombic cell.[9-12] This leads to a significant change in the environment of the Ag^+ cations: instead of the square anti-prism found in CsN_3, the orthorhombic distortion means that four of the terminal N-atoms are moved closer to the silver ions, resulting in two different Ag-N interactions. This gives rise to a distorted tetrahedral primary co-ordination environment around each cation formed by the azide termini within the same layer, while secondary Ag-N interactions exist between the layers (see Figure 6.2). The reduction in symmetry and the two crystallographically distinct N_3^- anions are reflected in the vibrational spectra: more vibrational modes are evident for AgN_3 than for the tetragonal forms of CsN_3 and TlN_3.[13, 14]

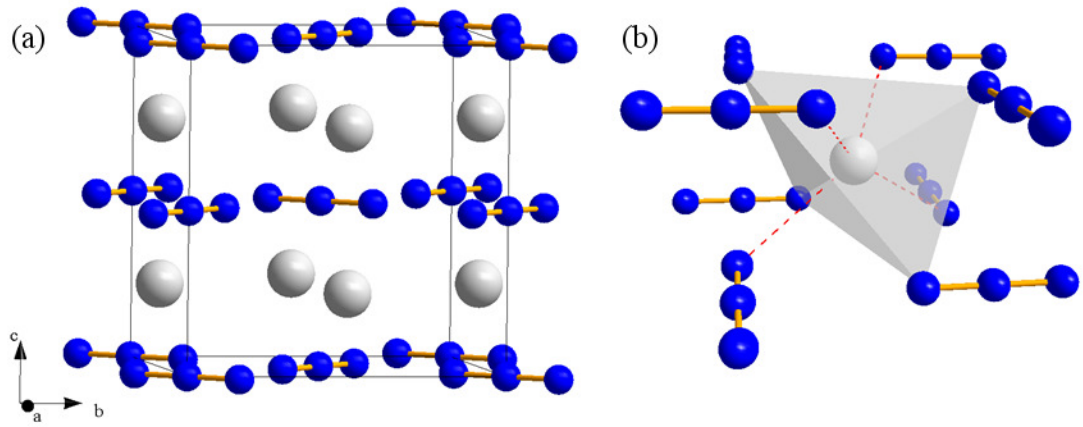

Figure 6.2 (a) Crystal packing in AgN_3 showing the similarity with the *I*4/*mcm* structures of CsN_3-II and TlN_3-II; and, (b) the cationic co-ordination environment – the primary 'tetrahedral' environment is shown in grey, while secondary Ag-N interactions are in red.

Raman studies of silver azide down to 10 K have shown that there is no phase transition to a low-temperature phase over this temperature range.[15] Warming to a maximum temperature of 443 K, however, results in a very sluggish phase transition to a monoclinic ($P2_1/c$) form that can be recovered to room temperature, as characterised by X-ray powder diffraction.[16] In this high-temperature form, the silver cation is surrounded by four nitrogen termini within the same layer (at distances ranging from 2.32 to 2.47 Å) in a distorted square geometry. Two further interactions (2.72 and 3.00 Å) with the azide groups above and below the plane of this layer give rise to a highly distorted 4 + 2 octahedral co-ordination environment (Figure 6.3). It is interesting to note that this phase transition is irreversible and that the high-temperature form is retained even after annealing the sample at 423 K.[16] This prompted the authors to perform density functional theory (DFT) calculations on both this form and the room temperature polymorph. Both represented minima on the calculated energy surface although it was not possible to determine which structure represented the global minimum.

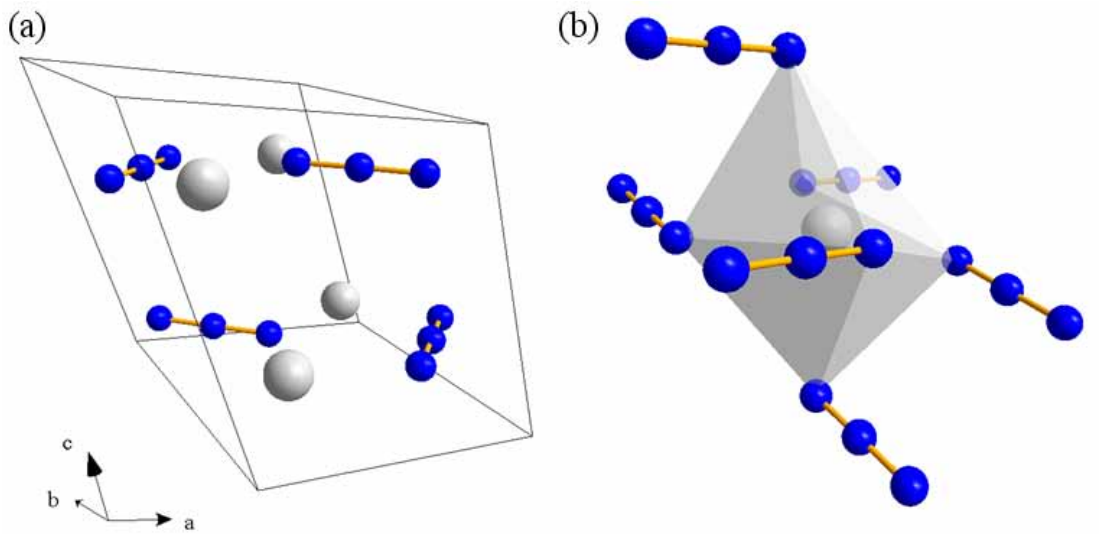

Figure 6.3 High-temperature modification of silver azide: (a) the crystal packing, and (b) the 4 + 2 co-ordination environment of the silver.

Experimental studies of the high-pressure behaviour of silver azide have been limited to a maximum pressure of 0.4 GPa – no evidence of a phase transition is observed from electrical conductivity [17] or spectroscopic measurements.[18] A DFT study on the structural and vibrational properties of AgN_3 under high pressure indicated the presence of an energetically favourable high-pressure phase above 7.0 GPa.[19] This high-pressure phase is predicted to adopt the tetragonal $I4/mcm$ symmetry of the CsN_3 and TlN_3 at ambient pressure and is considered to remain stable under hydrostatic compression to the limit of the study (500 GPa). No experimental study of silver azide has ever been undertaken in this pressure range and it was therefore a primary aim of the current work to obtain experimental evidence to

complement the theoretical predictions. Moreover the stability of the 'high-temperature form' at room temperature presents further evidence of the possibility of using a thermodynamic variable (such as temperature or, as reported herein, pressure) to obtain new materials that may be recovered to ambient conditions. This provided further motivation to investigate the high-pressure behaviour of silver azide.

6.1.3 $Pb(N_3)_2$

Four polymorphs of lead (II) azide have been identified, although only α-$Pb(N_3)_2$ has been thoroughly investigated crystallographically. The crystallisation of a monoclinic γ-form and a triclinic δ-form is reported to be favoured by low pH and/or the presence of additives such as polyvinyl alcohol. Both can be isolated as single crystals although no structural information (beyond tentative unit cell parameters) is available in the open literature.[20] Crystals of the monoclinic β-form, crystallised from aqueous solutions containing additives such as dextrin or by slow diffusion, are sufficiently metastable at ambient temperature such that they remain unchanged for years and may even be heated (473 K) for short periods with no obvious change. [21] However, the presence of small crystals of the more stable α-form results in a rapid solvent-mediated transition.[22] Detailed crystallographic investigations on β-$Pb(N_3)_2$ have been hampered by the tendency for spontaneous detonation during crystallisation.[23] As a result of the difficulties in growing single crystals of the different polymorphs, only the α-form has been structurally characterised.

The unit cell of the α-form was first determined by X-ray diffraction, although space group assignment was based primarily on the positions of the lead atoms.[21, 24, 25] In order to determine the atomic co-ordinates of the nitrogens accurately, and therefore to obtain an unambiguous space group, it was necessary to utilise neutron diffraction.[26-28] α-$Pb(N_3)_2$ crystallises in orthorhombic symmetry (*Pnma*) with four crystallographically distinct azide groups, all of which are distorted from the linear, symmetric configuration found in the ionic azides above. This is reflected in the complicated vibrational spectra, with numerous modes attributed to the different azide units.[14, 29] Bond lengths and angles within each of the azide groups and distances to the neighbouring Pb atoms are summarised in Figure 6.4.

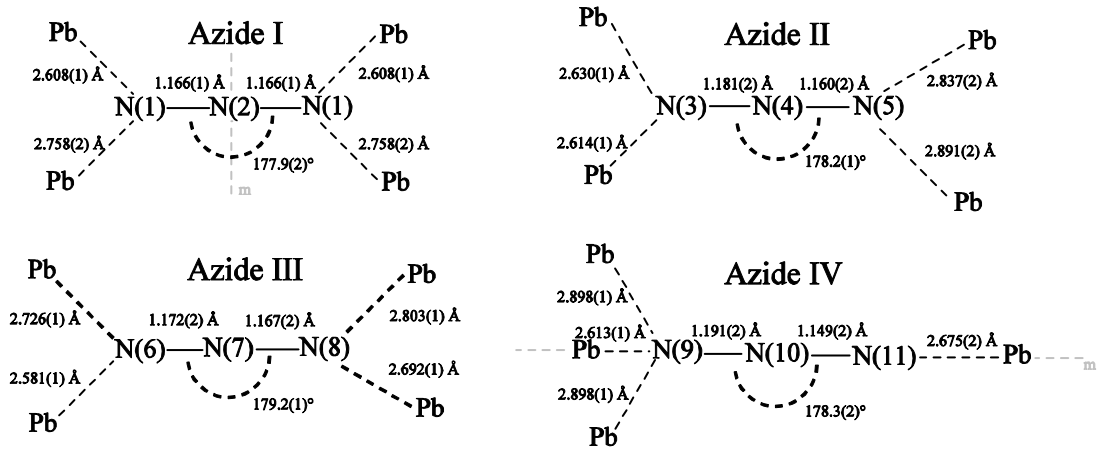

Figure 6.4 The four independent azide groups within α-$Pb(N_3)_2$ and their immediate Pb environment, as determined by Choi *et al.*[28] Azide I is situated over a mirror plane perpendicular to the N-N bonds, while IV occupies a mirror plane along with two Pb. The mirror planes are denoted m in the above scheme.

As illustrated in Figure 6.4, all of the azide groups are slightly bent and are asymmetric with the exception of azide I, which is situated across a mirror plane. Moreover the distortions within the azide groups are reflected in the Pb…N distances: the terminal nitrogen of the shortest N-N bond is in contact with only one neighbouring lead atom, while the other end of this azide group (with the longest N-N distance) is in close proximity to three Pb atoms. The asymmetric bonding within the azide groups and the related variation in Pb…N distances have been rationalised in terms of a degree of covalency between the metal and the azide groups.[28, 30]

Examination of the crystal packing shows that the azide ions arrange themselves into layers perpendicular to the crystallographic *c*-axis, with Pb atoms separating the layers. Azide types I and II occupy one sheet while the other is composed of azide types III and IV. Mauer *et al.* subsequently used this approach to explain the significant anisotropy in the thermal expansion of α-$Pb(N_3)_2$.[31] Over the temperature range 102 – 423 K, the linear expansion of the *c*-axis was found to be ~20 times that for the *b*-axis and four times that of the *a*-axis. They note that expansion in the direction normal to the azide layers would be expected to be larger than expansion within the layers, which would have to occur by either rotation or elongation of the individual azides. Weir *et al.* also note that the *c*-axis is the most compressible in α-$Pb(N_3)_2$ to a maximum pressure of 2.2 GPa.[32] It is important to note that neither group observed any phase transitions, although no structural refinements have been performed for $Pb(N_3)_2$ under extreme conditions.

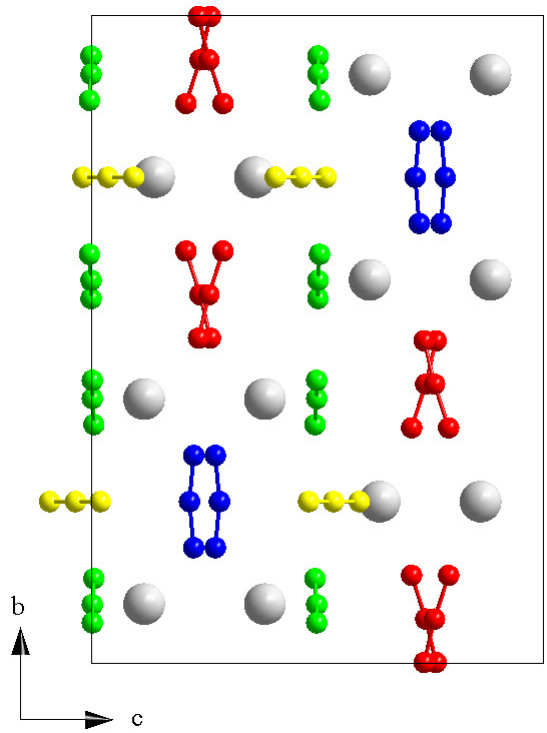

Figure 6.5 Crystal packing of α-$Pb(N_3)_2$, in which each independent azide group is clearly distinguished: Type I (blue), Type II (red), Type III (green) and Type IV (blue).

It was therefore proposed to obtain high quality neutron powder diffraction data during the compression of α-$Pb(N_3)_2$ to a maximum pressure of 5.74 GPa in order to understand qualitatively the compression mechanism, to obtain an equation of state for this material (for comparison with *ab initio* calculations [33]) and to investigate any new high-pressure forms.

6.2 Aims

Reference to Table 6.1 not only shows the structural variety of these compounds under ambient conditions, but also highlights the lack of structural information under extreme conditions, particularly at elevated pressures. The aim of the current study is therefore to explore the effect of high pressure on ammonium azide, silver azide and lead(II) azide by neutron powder diffraction. The results of these studies will provide valuable information on the compressibilities of these materials, as well as identifying and characterising any high-pressure polymorphs that may be obtained.

Polymorph	Space Group	*a* (Å)	*b* (Å)	*c* (Å)	*α* (°)	*β* (°)	*γ* (°)	Atomic positions?	*P*/*T* conditions	Ref.
NH_4N_3	*Pmna*	8.948(3)	3.808(2)	8.659(3)	90	90	90	Yes	Ambient *P*/*T*	[3]
α-AgN_3	*Ibam*	5.600(1)	5.980(6)	5.998(1)	90	90	90	Yes	Ambient *P*; *T* < 443 K	[11]
β-AgN_3	$P2_1/c$	6.0756(2)	6.1663(2)	6.5729(2)	90	114.19(0)	90	Yes	Ambient *P*; *T* > 443 K Recovered to ambient *P*/*T*	[16]
α-$Pb(N_3)_2$	*Pnma*	6.63	16.25	11.31	90	90	90	Yes	Ambient *P*/*T*	[24],[28]
β-$Pb(N_3)_2$	-	18.31	8.88	5.12	90	107.5	90	No	Ambient *P*/*T*	[22]
γ-$Pb(N_3)_2$	-	12.060	10.507	6.505	90	95.75	90	No	Ambient *P*/*T*; low pH/additives	[20]
δ-$Pb(N_3)_2$	-	13.163	10.532	6.531	90.53	98.12	112.67	No	Ambient *P*/*T*; low pH/additives	[20]

Table 6.1 Structural information for all polymorphs of the inorganic azides (where no esd is tabulated, no values were given in the primary literature).

6.3 Experimental

6.3.1 Materials

Due to concerns over their sensitivity to detonation, samples (*ca* 100 mg) of AgN_3 and $Pb(N_3)_2$ were prepared at the ISIS Neutron and Muon Source immediately prior to the high-pressure neutron diffraction experiments. AgN_3 was prepared by mixing equimolar solutions of silver nitrate and sodium azide at room temperature and subsequent washing with deionised water. Lead(II) azide was produced by the solution-phase reaction of $Pb(NO_3)_2$ and NaN_3 (purchased from Sigma-Aldrich, 99.5% purity). NH_4N_3 was prepared by the metathetic reaction of ammonium chloride and sodium azide as reported by Richter.[34] Equimolar amounts of NH_4Cl and NaN_3 were distilled with a small quantity of water; the product NH_4N_3 volatised at 433 K with water vapour and solidified in the condenser tube. Recovery of small crystallites of NH_4N_3 was complicated by its propensity to deliquesce at room temperature – the pure product was precipitated from aqueous solution at ~ 278 K and removed to a desiccator for storage. ND_4N_3 for neutron powder diffraction was prepared by the analogous reaction of ND_4Cl and NaN_3 (in D_2O) by Dr P. Szilagyi (School of Chemistry, University of Edinburgh).

Sample purity was confirmed by neutron powder diffraction at minimal sample pressure for AgN_3, $Pb(N_3)_2$ and ND_4N_3.

6.3.2 High-Pressure Neutron Powder Diffraction

High-pressure neutron powder diffraction data were collected using the PEARL/HiPr diffractometer at the UK spallation neutron source, ISIS, at the STFC Rutherford Appleton Laboratory. Polycrystalline samples of each compound under investigation (ND_4N_3, AgN_3 and $Pb(N_3)_2$) were loaded, in turn, into an encapsulated TiZr gasket [35] with perdeuterated methanol:ethanol (4:1) as pressure-transmitting medium and Pb as pressure calibrant.[36] The capsule assembly was then compressed with a type V3b Paris-Edinburgh (P-E) press equipped with standard single toroid anvils with cemented WC cores (Ni binder).[37] The P-E press ram pressure was monitored and varied by means of a computer-controlled hydraulic system.

Time-of-flight (ToF) neutron powder diffraction data were collected using the $2\theta = 90°$ detectors with a transverse (through-anvil) scattering geometry. The resulting summed pattern was then normalised with respect to the incident beam monitor and the scattering from a standard vanadium calibration sample. Lastly, the diffraction pattern intensity scale was corrected for the wavelength and scattering-angle dependence of the neutron attenuation

by the anvil (WC) and gasket (TiZr) materials. Full-profile Rietveld refinements of the ToF neutron powder diffraction patterns were carried out using the GSAS package, in which a convolution of Gaussian (with coefficient σ_1) and Lorentzian (γ_1) functions was used to describe peak profiles (GSAS ToF profile 3).[38] Details of any restraints applied (when necessary) during refinement will be outlined in the relevant sections below.

6.4 Results and Discussion

6.4.1 NH_4N_3

High-Pressure Neutron Diffraction Study of ND_4N_3

In the first ever such study, the high-pressure polymorphism of ND_4N_3 was investigated by neutron powder diffraction to a maximum pressure of 4.9 GPa. The diffraction patterns collected during this experiment are presented in Figure 6.6. In order to ensure sample purity it was necessary to collect a diffraction pattern at low initial load (6 tns, sample pressure = 0.07 GPa). Full-profile Rietveld refinement confirmed the orthorhombic structure and the data were of such high quality (after 2 hours exposure) that it was possible to refine the thermal parameters of the deuterium atoms anisotropically. Figure 6.7 shows how the thermal ellipsoids of two of the deuteriums are elongated along the direction of the hydrogen bonds to the nearest azide anions, while the longest axis in the ellipsoids of the other two are normal to their hydrogen bonds. This results in a scissor-type motion of the tetrahedral cations. As has been observed in previous studies, the tetrahedra do not rotate freely about their positions in the lattice.

Shorter data collection times were utilised in later runs in order to maximise the pressure range studied; thermal parameters at these pressures were therefore refined isotropically. As is evident from Figure 6.6, the α-form remains stable upon compression to 2.39 GPa, but at the next pressure (2.6 GPa) the diffraction pattern changes dramatically. This pattern persisted to the highest pressure studied (4.9 GPa). It should be noted that, since it has not been possible to carry out Rietveld refinements of the patterns collected for this high-pressure β-form, pressures have been determined using estimations of the *d*-spacings of the Pb (200) and (111) peaks and will therefore have a larger error associated with them.

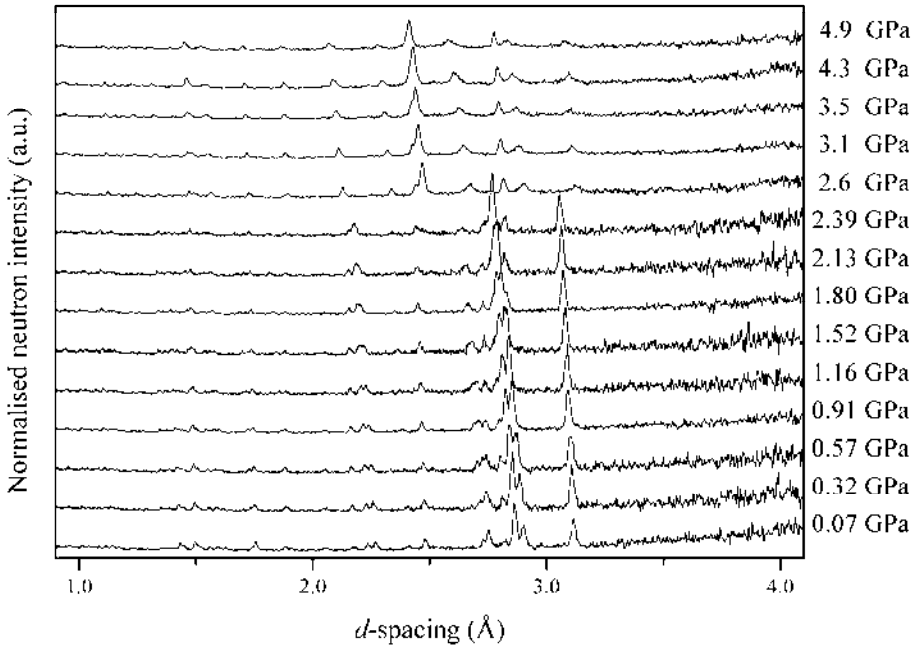

Figure 6.6 Multiplot of the neutron powder diffraction patterns collected for ND_4N_3. Since it has not been possible to perform full-profile Rietveld refinements on the patterns collected for the high-pressure β-form, pressures have been estimated based on the position of the Pb (002) and (111) peaks.

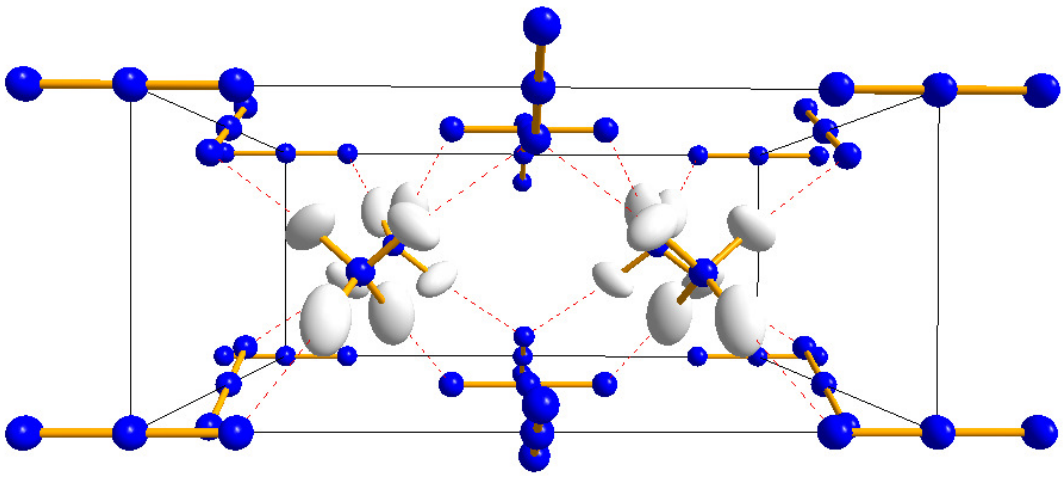

Figure 6.7 Crystal structure of ND_4N_3 at 0.07 GPa, in which the anisotropic displacement parameters of the deuterium atoms have been shown (50 % level). The thermal parameters of the nitrogen atoms were refined isotropically.

The unit cell parameters determined during the compression of α-ND_4N_3 have been tabulated in Table 6.2 and are presented graphically in Figure 6.8. The relative compressibilities of the unit cell axes are also presented. This shows that the *c*-axis is the least compressible, while the *b*-axis is the most compressible. Both of these features may be explained by a

compression mechanism which involves the rotation of the azide anions that lie normal to the *a*-axis (Type II). During the compression of α-ND_4N_3 these azides become more parallel with the *c*-axis: this would therefore counter the effects of pressure on the *c*-axis while also explaining the more rapid decrease in the *b*-axis as the wave-like planes of N_3^- anions flatten out. The rotation of these azides with respect to the *c*-axis is plotted in Figure 6.9. Compression along the *a*-axis would increase the interactions between the terminal N-atoms of Type I azides and the central N-atom of Type II, but this is balanced by repulsion between the tetrahedral cations. It is also interesting to note that during compression the central nitrogen atoms of the NH_4^+ ions become more eclipsed; using the *ac*-plane as reference, the degree of stagger has been calculated at each pressure and is plotted in Figure 6.10.

P (GPa)	*a* (Å)	*b* (Å)	*c* (Å)	*V* (Å^3)	wR_p
0.07	8.9282(18)	3.8033(8)	8.6646(19)	294.22(7)	0.065
0.32	8.9052(18)	3.7764(8)	8.6510(19)	290.93(7)	0.121
0.57	8.8745(18)	3.7530(7)	8.6405(18)	287.78(7)	0.109
0.91	8.8421(12)	3.7242(5)	8.6231(12)	283.96(5)	0.071
1.16	8.8118(19)	3.6964(8)	8.6142(18)	280.58(8)	0.138
1.52	8.7797(19)	3.6713(8)	8.6056(18)	277.39(8)	0.152
1.80	8.7454(11)	3.6474(5)	8.5924(11)	274.08(5)	0.089
2.13	8.7093(18)	3.6219(7)	8.5883(17)	270.91(7)	0.220
2.39	8.6517(20)	3.5954(7)	8.5969(20)	267.42(7)	0.173

Table 6.2 Unit cell parameters obtained during the compression of α-ND_4N_3.

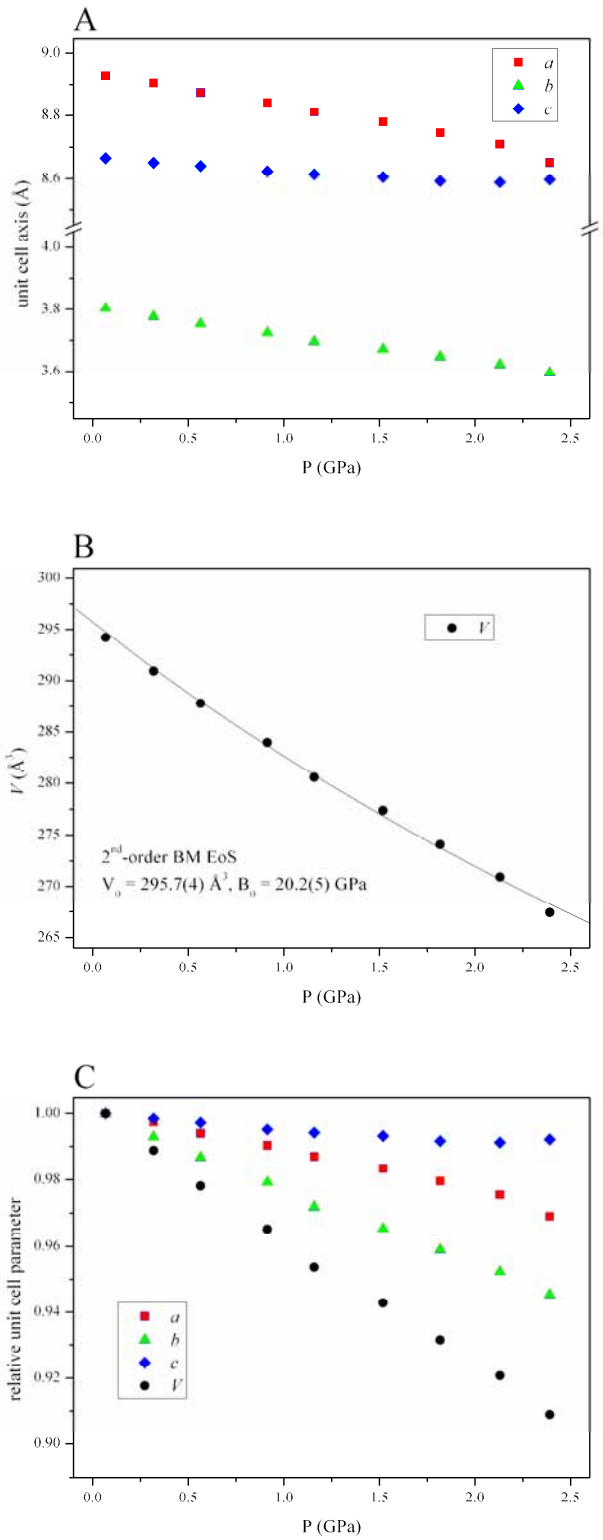

Figure 6.8 (a) Contraction of the unit cell parameters of α-ND_4N_3 indicating that the *a*- and *c*-axes become more equivalent at higher pressures; (b) the 2nd-order Birch-Murnaghan *PV*-plot for compression of α-ND_4N_3; and, (c) the relative contraction of the unit cell parameters.

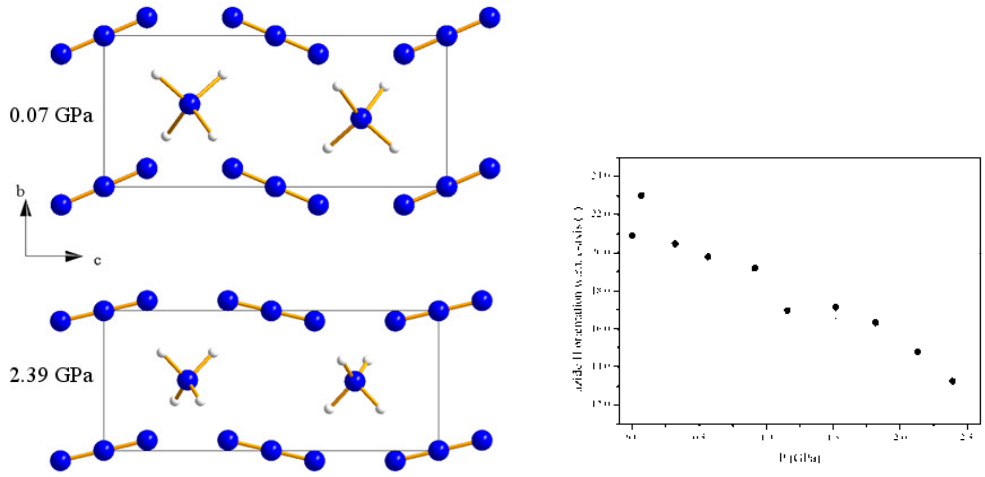

Figure 6.9 (a) Rotation of azide (Type II) w.r.t. *c*-axis between 0.07 and 2.39 GPa. This has been represented graphically in (b) [e.s.d. = 0.6°].

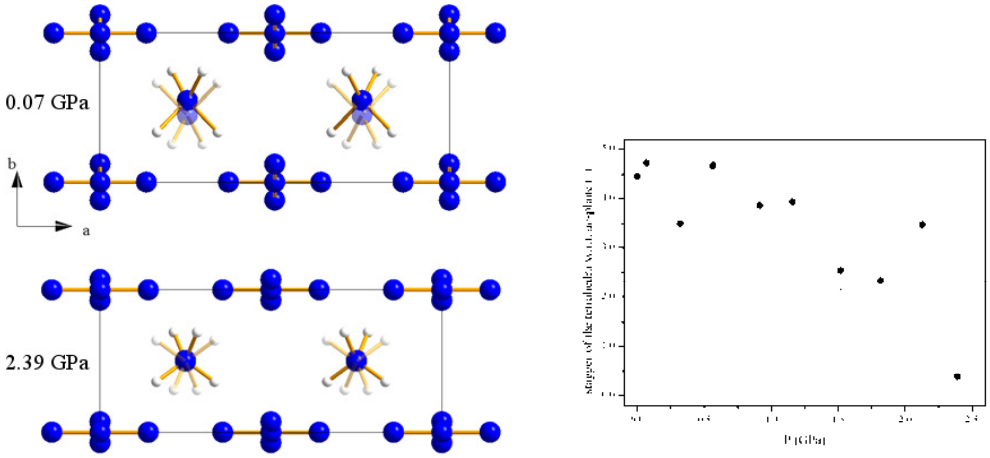

Figure 6.10 (a) Stagger of tetrahedral cations – the foremost tetrahedra have been lightened to allow them to be distinguished. This gradual reduction in the tetrahedral stagger during compression has also been represented graphically in (b) [e.s.d. = 0.4°].

Data-points in the plot of the normalised pressure (F_E) against Eulerian strain (f_E) were found to lie on a horizontal line indicating that the compression of unit cell volume would be adequately described by a 2nd-order Birch-Murnaghan EoS.[39] The coefficient were calculated to be: V_0 = 295.7(4) Å^3 and B_0 = 20.2(5) GPa and are in good agreement with the experimentally determined volume at ambient pressure (295.05 Å^3) [3] and the intercept of the *Ff*-plot (19.7).

The dramatic change in the neutron powder diffraction patterns upon increasing sample pressure from 2.39 GPa to 2.6 GPa was indicative of a phase transition. This new β-ND_4N_3 was then compressed to a maximum pressure of 4.9 GPa; no further phase transitions were

observed. Moreover this high-pressure polymorph was observed to persist during decompression to 2.1 GPa, *i.e.* below the upstroke transition pressure; the sample was observed to have transformed to the α-form at 1.52 GPa.

Unfortunately it has not been possible to obtain an unambiguous indexing for the high-pressure β-form. It should be noted that, despite the apparent convergence of the unit cell a- and *c*-axis during compression of the α-form, Le Bail refinement of the patterns collected for the high-pressure form indicates that this transition does not appear to result in a tetragonal unit cell. The process of obtaining unambiguous unit cell indexings is complicated based on neutron powder diffraction patterns due to the limited range of *d*-spacing accessible and the overlap of sample peaks with peaks due to the Pb pressure calibrant and WC and Ni from the PE-press anvils. An analogous powder diffraction study using synchrotron radiation is therefore planned to obtain complementary data on this high-pressure phase. It is also hoped that single crystals of this material are sufficiently stable under ambient conditions to permit their loading into a diamond-anvil cell for X-ray single-crystal diffraction experiments. Moreover, an X-ray study on the hydrogenous material would also highlight any deuteration effects on the transition pressure or compression mechanism.

Summary: ND_4N_3

The structure of ammonium azide has been investigated under high pressure. The compression of the α-form, which remains stable to a pressure of 2.39 GPa, is characterised by a rotation of half of the azide anions and an alignment of the tetrahedral cations. The β-form, which is still to be structurally characterised, remains stable to the maximum pressure studied (4.9 GPa) and displays hysteresis during decompression. Complementary X-ray powder diffraction studies on the hydrogenous material are planned and the possibility of loading single crystals of NH_4N_3 into a diamond-anvil cell for high-pressure single-crystal X-ray diffraction is currently being explored.

6.4.2 AgN_3

The interesting polymorphism of silver azide at high temperature (and the recovery of this high-temperature form to ambient pressure) motivated the study of this material at high pressure by means of neutron powder diffraction. A freshly prepared sample of AgN_3 was therefore compressed to a maximum of 5.17 GPa, which was sufficient pressure to induce a phase transition (observed at 0.80 GPa). This is in contrast to theoretical predictions of the same phase transition occurring at 7.0 GPa.[19] A multiplot of the neutron powder diffraction patterns collected throughout this study is shown in Figure 6.11.

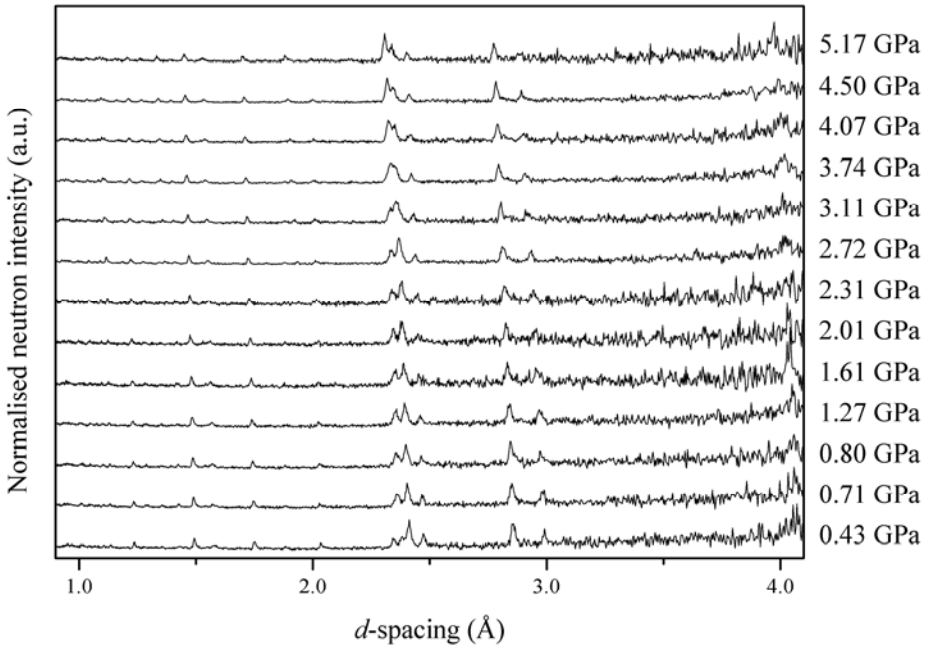

Figure 6.11 Multiplot of the neutron powder diffraction patterns collected during the compression of AgN_3.

Using the ambient pressure α-structure (orthorhombic, *Ibam*) it was possible to carry out full-profile Rietveld refinements on the patterns collected at 0.43 and 0.71 GPa. In order to assess the compression of this phase fully, these data are presented along with the ambient pressure unit cell parameters reported by Guo *et al*. in Table 6.3. This clearly shows that, while the orthorhombic *c*-axis shows limited compressibility (~1%), the *b*-axis shortens dramatically (~4%) and the *a*-axis actually lengthens. The contraction of the *b*-axis may be rationalised in terms of a shortening of the interplanar distance, which one would expect to be more compressible than either of the intraplanar axes. Interestingly, however, the expansion along *a* is not due to any rotation of the azide anions; the angle between the long axis of the azide and the *a*-axis does not change significantly in this pressure region. The relative change in the unit cell parameters, however, does result in a change in the co-ordination of the silver cations. Rather than there being two very distinct Ag-N distances, as in the ambient pressure structure, by 0.71 GPa the silver co-ordination sphere becomes almost, but not quite, a perfect square antiprism. The interplanar distance shortens from 2.80 Å at 0.0 GPa to 2.69 Å at 0.71 GPa; the intraplanar distance meanwhile increases from 2.56 to 2.62 Å.

P (GPa)	a (Å)	b (Å)	c (Å)	V (Å^3)	wR_p
0.00	5.600(1)	5.980(6)	5.998(1)	200.86(20)	Ref. [11]
0.43	5.659(2)	5.830(3)	5.9701(13)	196.95(8)	0.114
0.71	5.704(3)	5.760(3)	5.9512(14)	195.52(8)	0.118

Table 6.3 Unit cell parameters obtained during compression of α-AgN_3, presented alongside literature values obtained at ambient pressure (293 K).

This continuing distortion, or rather removal of an orthorhombic distortion, by the application of pressure eventually results in a phase transition to the tetragonal structure of γ-AgN_3 (*I*4/*mcm*). This structure is analogous to the structures adopted by CsN_3 and TlN_3 at ambient conditions and NaN_3 at elevated temperatures and pressures. It was therefore relatively straightforward to perform Rietveld refinements on all of the diffraction patterns collected for this form, up to a maximum pressure of 5.17 GPa. The unit cell parameters obtained during these refinements are presented in Table 6.4 and Figure 6.12.

P (GPa)	a, b (Å)	c (Å)	V (Å^3)	wR_p
0.80	5.7239(11)	5.9338(14)	194.41(7)	0.110
1.27	5.7146(11)	5.9231(14)	193.43(7)	0.106
1.61	5.7087(17)	5.9026(20)	192.36(11)	0.310
2.01	5.6965(15)	5.8818(20)	190.86(9)	0.223
2.31	5.6885(17)	5.8727(20)	190.03(11)	0.306
2.72	5.6804(12)	5.8483(15)	188.71(8)	0.109
3.11	5.6714(13)	5.8183(16)	187.14(8)	0.165
3.74	5.6637(13)	5.7936(17)	185.84(9)	0.120
4.07	5.6565(14)	5.7820(18)	185.00(9)	0.162
4.50	5.6431(9)	5.7695(13)	183.73(6)	0.130
5.17	5.6191(15)	5.7509(19)	181.58(10)	0.271

Table 6.4 Unit cell parameters during compression of γ-AgN_3

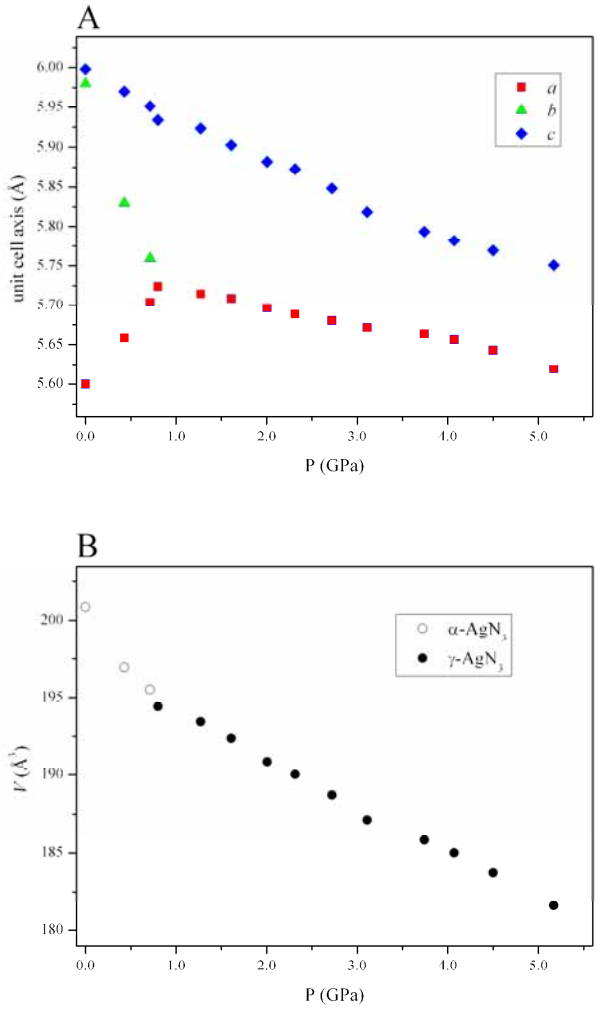

Figure 6.12 (a) Variation of the unit cell parameters throughout compression, highlighting the orthorhombic/tetragonal transition at 0.80 GPa; and, (b) compression of the unit cell volume across the α → γ transition.

As in the other tetragonal azides, the Ag^+ and N_3^- ions are arranged in layers normal to the *c*-axis; within these layers the azide ions lie perpendicular to their nearest neighbours. It is therefore not surprising that the *c*-axis is the most compressible (Figure 6.13). The compression of the *ab*-plane manifests itself in the shortening of the $N_{central}$-$N_{terminal}$ interactions between neighbouring azides - in this pressure range the azides do not rotate and thus the 4-fold rotational symmetry is maintained. Moreover, a result of the phase transition is that the co-ordination environment of the cations becomes a regular square-antiprism with 8 equivalent Ag-N interactions (2.67 Å at 0.80 GPa). This arrangement is maintained throughout compression of the γ-form: the contraction of the *c*-axis is mirrored in the shortening of these interactions.

An interesting feature of the compression of γ-AgN_3 is the slightly convex nature of the *PV*-plot (Figure 6.13), which indicates that the structure becomes more compressible at higher pressures. Although rare, such behaviour has been observed during the compression of network solids, particularly those that have been noted to exhibit negative thermal expansion, such as $Zn(CN)_2$ [40] and ZIF-8, a zinc imidazolate framework.[41] The exact reasons for this behaviour in the case of silver azide are, as yet, unknown but this anomalous compression behaviour is most affected by the contraction of the *c*-axis. This is also reflected in the variation of the interplanar Ag…Ag and Ag-N interactions. One may therefore suggest that argentophilic (Ag…Ag) interactions compound the applied compression along the *c*-axis leading to a greater than expected contraction along this direction. In order to be confident in this conclusion, however, it would be advisable to extend the pressure range of the current study to validate the current observations and to examine the compression mechanism at higher pressures. This would also allow further refinement of the EoS for γ-AgN_3. Furthermore, DFT calculations have been planned to investigate whether it is possible to re-create this anomalous compression behaviour computationally.

The data presented in Figure 6.13 have been fitted to both a 3rd-order Birch-Murnaghan [B_0 = 70(3) GPa, B' = -1.4(14)] and a Vinet [B_0 = 71(4) GPa, B' = -2.5(19)] equation of state.[42] As for TlN_3-III above, the value of V_0 (194.14 Å^3) has been fixed to the experimentally determined volume at 0.80 GPa; all subsequent pressures have been scaled to this value. The large errors associated with the values of B' are a reflection of the relatively poor fit to the data. Both equations, however, accurately describe the marginally convex volume curve (negative B') and show relatively good agreement on the values of the bulk modulus. Should the negative values of B' be verified by future studies, this would mean that AgN_3 is dramatically more resistant to compression than the ionic azides above. This has previously been attributed to the degree of covalency displayed by silver azide, in contrast to the purely ionic alkali metal azides.[19]

In order to test the sensitivity of the coefficients B_0 and B' to the value of V_0, 3rd-order Birch-Murnaghan and Vinet equations of state were also fit using the unit cell volume of α-AgN_3 (200.86 Å^3 [11]) at atmospheric pressure as V_0. Furthermore, in a third set of least-squares regression the value of V_0 was refined. A summary of these regressions may be found in Table 6.5. It is interesting to note that, of the three case presented, the worst fit to the *PV* data is obtained by fixing V_0 to be the same as in the α-form, although this does result in values of B_0 and B' (*ca* 27 GPa and 15, respectively) that are in accordance with the other metal azides presented in this work. The quality of the fit improves markedly upon allowing

V_0 to refine (for example, R_w is reduced from 4.735% to 1.918% in the 3rd-order Birch-Murnaghan EoS) although this is accompanied by an equally dramatic increase in B_0 (26.2 to 60 GPa). Furthermore, one may suggest that the error associated with the extrapolation of V_0 may be much larger than that indicated by the standard error presented in Table 6.5 due to the highly-correlated nature of the coefficients of these regressions. Such observations suggest that extreme caution should be taken when fitting equations of state, particularly to high-pressure phases for which V_0 cannot be accurately determined. For this reason, it is suggested that this study be repeated with particular emphasis on the collection of high-quality diffraction data at low pressure, in order to obtain a sufficient number of *PV* data-points for a reliable equation of state.

Assumption	Model	Coefficients	Fitting Statistics
$V_0 = V_{0.80\ GPa}$	3rd-order Birch-Murnaghan	V_0 = 194.14 Å^3 (fixed) B_0 = 70(3) GPa B' = -1.4(14)	R_u = 3.601% χ^2_u = 0.0125 R_w = 4.118% χ^2_w = 3.6983
	Vinet	V_0 = 194.14 Å^3 (fixed) B_0 = 71(4) GPa B' = -2.5(19)	R_u = 3.566% χ^2_u = 0.0122 R_w = 4.072% χ^2_w = 3.6114
$V_0 = V_{0(\alpha\text{-form})}$	3rd-order Birch-Murnaghan	V_0 = 200.86 Å^3 (fixed) B_0 = 26.2(25) GPa B' = 17(4)	R_u = 3.901% χ^2_u = 0.0251 R_w = 4.735% χ^2_w = 7.4663
	Vinet	V_0 = 200.86 Å^3 (fixed) B_0 = 27.9(21) GPa B' = 13.2(19)	R_u = 3.987% χ^2_u = 0.0273 R_w = 4.968% χ^2_w = 8.2143
V_0 refined	3rd-order Birch-Murnaghan	V_0 = 197.2(4) Å^3 B_0 = 60(5) GPa B' = 1.3(15)	R_u = 1.918% χ^2_u = 0.0063 R_w = 2.187% χ^2_w = 1.9145
	Vinet	V_0 = 197.2(4) Å^3 B_0 = 60(6) GPa B' = 0.9(20)	R_u = 1.925% χ^2_u = 0.0063 R_w = 2.185% χ^2_w = 1.9134

Table 6.5 Coefficients of the equations of state determined for γ-AgN_3 highlighting their dependence on the assumptions used. The quality of the fit in each case may be assessed by comparison of the fitting statistics calculated during the least-squares regression (obtained from the EoSFIT output file).[39]

The current experimental study provides complementary data to a previous computational study on the structural properties of silver azide up to 500 GPa. While this theoretical study correctly predicts a phase transition to the tetragonal (*I*4/*mcm*) structure, the transition pressure was grossly overestimated (7 GPa compared to 0.8 GPa in this work). Furthermore the calculations do not correctly represent the compression of the unit cell volume or the individual parameters: the expansion of the orthorhombic *a*-axis is not predicted to occur until > 5 GPa; the *c*-axis in γ-AgN_3 is predicted to be the short axis; and the value of B' is predicted to be positive. This should therefore underscore the importance of carrying out

experimental high-pressure studies on these materials, in order to test rigorously and, ultimately, improve computational models of their properties under extreme conditions.

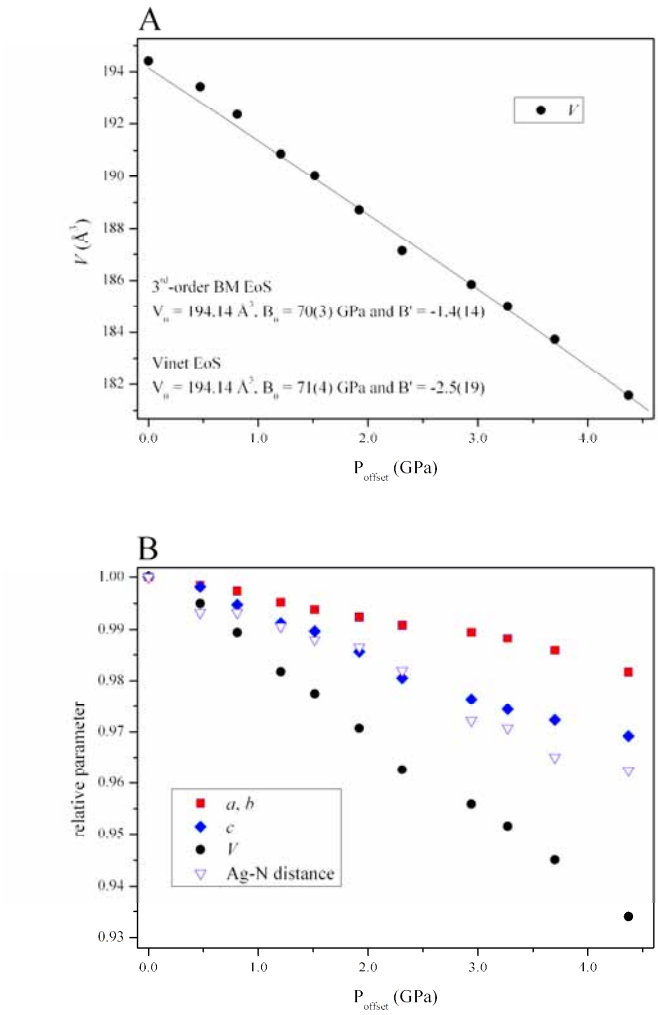

Figure 6.13 (a) Compression of γ-AgN_3 – the marginally convex character to the *PV*-plot is reflected in the negative values of B' for both the 3rd-order Birch-Murnaghan and Vinet equations of state; and, (b) the relative compression of the unit cell axes and volume presented alongside the contraction of the Ag-N distance.

The observation that the high-temperature β-form could be recovered to ambient temperature meant that the decompression of the γ-form was of great interest in the present study. Unfortunately the time constraints of the neutron diffraction experiment meant that data could not be collected at a series of pressures during decompression. It was, however, possible to collect a diffraction pattern of the sample at atmospheric pressure (shown in Figure 6.14 alongside patterns collected for both the α- and γ-forms). The diffraction pattern collected at 0 GPa shows no Bragg peaks other than the Pb, WC and Ni from the sample environment. Despite this, the observation that the sample remained in the capsule during

decompression is indicative of sample amorphisation during decompression, rather than leakage from the gasket. Visual inspection of the recovered sample found that it had darkened considerably from the initial loading; this grey colouration was found to permeate the whole sample and was not limited to a surface effect. A significant rise in vacuum pressure in the sample chamber was also observed upon reducing the load to below 2 tns, suggesting the release of a gaseous decomposition product.

The reason for this apparent amorphisation is not yet clear, although one would not expect the subtle transition from the tetragonal γ-form to the related orthorhombic α-form to cause a great deal of structural rearrangement. However, at this time it is not possible to exclude the possibility of a further polymorph obtained during decompression. An alternative mechanism may be the photolytic decomposition of AgN_3 (resulting from the cumulative effects of γ-radiation) to produce amorphous Ag(s) and N_2(g). Throughout the course of the experiment the sample may have been exposed to periodic flashes of γ-radiation from the spallation target, although one may reasonably expect a considerable portion of this to have been absorbed by the sample environment. In fact, it is perhaps more likely that the sample itself becomes a source of γ-radiation due to neutron absorption by the silver atoms and their subsequent decay.

Numerous silver salts, particularly the silver halides, have been observed to be susceptible to photolytic decomposition to metallic silver.[43-45] Indeed the effect of radiation absorption on the decomposition of silver azide has been documented for over a century [46], although recent interest has focussed on the targeted precipitation of silver nanoparticles by exposure of silver salts, such as AgN_3, to high-energy radiation.[47, 48] It is therefore reasonable to suggest that exposure of the sample to γ-radiation may result in an accumulation of crystal defects that would impact greatly on the stability of the crystal lattice during decompression.

Of course, the observed amorphisation upon decompression may be attributable to a combination of the mechanical and chemical processes outlined. It would therefore be highly desirable to conduct a more detailed decompression study to highlight: any further phase transitions; the development of crystal strain within the sample; or, any changes in sample composition (by the reduction of Bragg peak intensities).

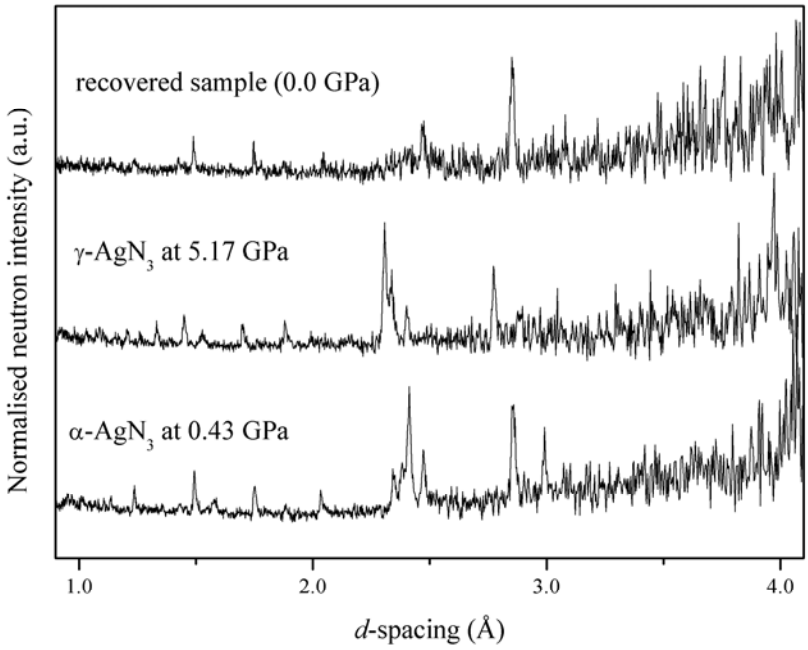

Figure 6.14 Comparison of the neutron powder diffraction pattern collected after decompression with those collected for the α-form (at the lowest pressure, 0.43 GPa) and the γ-form (immediately prior to decompression, 5.17 GPa). Apart from contributions from the Pb pressure marker and the WC and Ni from the sample environment, no Bragg peaks are observed.

Summary: AgN_3

The high-pressure polymorph of silver azide (γ-AgN_3) has been structurally characterised. This is the first experimental evidence for a form that was predicted theoretically, although several discrepancies arise between the theoretical study and the results presented herein (primarily the transition pressure). γ-AgN_3 has been found to adopt the same space group (*I*4/*mcm*) as the azides of the larger alkali metals at ambient conditions and has been shown to be the result of the gradual reduction of an orthorhombic distortion by the application of pressure.

The application of pressure to the γ-form is manifested mainly in the contraction of the tetragonal *c*-axis by reduction of the interplanar distance and is perhaps enhanced by increased argentophilic interactions between the layers. This results in a slightly convex compression curve (characterised by a negative value of B'), although this should be verified by further study. A more detailed study of the decompression of γ-AgN_3 and characterisation of the recovered product would provide a valuable insight into the observed amorphisation.

6.4.3 $Pb(N_3)_2$

The last of this series of inorganic azides to be investigated under high pressure was lead(II) azide. After obtaining a high-quality neutron powder diffraction pattern at minimal applied load (sample pressure of 0 GPa as determined by Pb calibrant) to confirm sample purity, the compression of the α-form was studied to 2.38 GPa. At the next pressure (2.60 GPa) a new reflection was observed at ~2.36 Å, although there was very little change in the rest of the pattern. This reflection persisted, and in fact grew in intensity, during further compression to the highest pressure studied (5.8 GPa), as is shown in Figure 6.15. Subsequent decompression to ambient pressure confirmed that the sample had not undergone decomposition and that this phase transition to a distinct ε-form is reversible. No additional peaks were observed during the Rietveld refinement of the ambient pressure pattern using the α-$Pb(N_3)_2$ structural model.

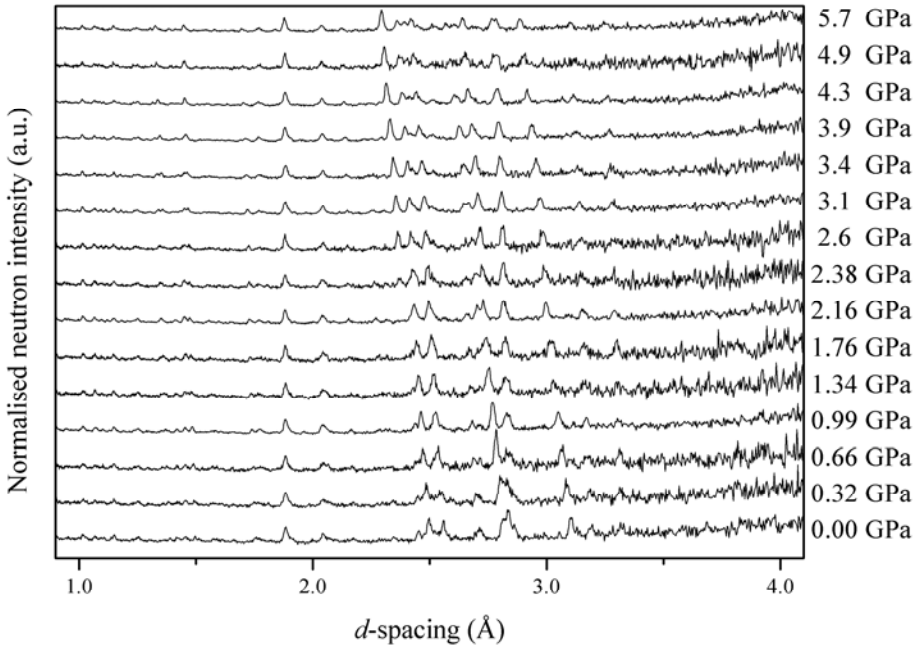

Figure 6.15 Multiplot of the neutron powder diffraction patterns collected for $Pb(N_3)_2$ up to 5.7 GPa. Since it has not been possible to perform full-profile refinements on the ε-$Pb(N_3)_2$ patterns (*i.e.* above 2.6 GPa), the pressures in these runs have been estimated by the position of the Pb (200) peak.

The structure is the most complex of the series – $Pb(N_3)_2$ contains four independent azide groups, none of which is completely linear and symmetric. This structural complexity, along with the limited range of *d*-spacing accessible during a high-pressure neutron diffraction experiment, meant that Rietveld refinement of the patterns collected during the compression

of the α-form was laborious. Refinements were initially attempted without the application of restraints to bond distances and bond angles, an approach that has been possible for all other refinements in this chapter. Unfortunately, this resulted in chemically unreasonable values for some N-N bond distances (for example, bond distances less than 1.00 Å in some cases).

In order to balance the need for the structure to remain chemically reasonable with an accurate description of the intermolecular and intramolecular interactions it was then decided to apply restraints to the bond distances and bond angles of the azide groups, with large enough standard deviations to allow sufficient variation to indicate any structural effects of the applied pressure. The N-N bond distances were restrained to 1.165(10) Å, while the N-N-N bond angles in azides II-IV were restrained to be 180(2)°. The bond angle within azide I (N1-N2-N1) was restrained by including a dummy atom (N1') as in TlN_3-IV.[49] However, refinements of the powder patterns did not converge successfully when these restraints were applied, particularly at higher pressures. On closer inspection this was found to be due to violation of the bond angle restraints that prevented convergence of the refinements.

It was therefore decided to conduct the refinements without the bond angle restraints, while maintaining the restraints applied to the bond distances. In this case the refinements successfully converged and the resulting bond distances and angles remained chemically reasonable throughout.

In order to critically assess the non-linearity of the azide units, a further refinement strategy that was employed was to restrain the distance between the two termini of each azide (II – IV) to be comparable to the ambient pressure distance, 2.340(20) Å. By the application of this restraint, in conjunction with the N-N bond distance restraint outlined above, it was hoped that linearity could be maintained without the requirement of an explicit angle restraint. In this case, convergence was successfully attained although the values of χ^2 and wR_p increased marginally (see Table 6.6 for a summary of all the refinement procedures). Despite these restraints, however, it should be noted that the azide groups still deviate significantly from linearity. For example, azide III adopts an angle of 172° and therefore one can conclude that this procedure is no more appropriate than the application of bond restraints alone, although this may be worthwhile for better quality data-sets. For this reason, the latter refinement procedure has been applied to all of the high-pressure data collections for α-$Pb(N_3)_2$. The values of the unit cell parameters obtained in this way can be found in Table 6.7 and Figure 6.16.

Bond Restraint $N_{terminal}$-$N_{central}$	Angle Restraint N-N-N (II – IV)	Length Restraint $N_{terminal}\ldots N_{terminal}$ (II – IV)	Quality of Fit
-	-	-	$\chi^2 = 1.140$ $wR_p = 0.0447$
1.165(10) Å	-	-	$\chi^2 = 1.142$ $wR_p = 0.0457$
-	180(2)°	-	did not converge
1.165(10) Å	180(2)°	-	did not converge
1.165(10) Å	-	2.340(20) Å	$\chi^2 = 1.146$ $wR_p = 0.0459$
1.165(10) Å	180(2)°	2.340(20) Å	did not converge

Table 6.6 Restraints applied during the refinement of the neutron powder diffraction pattern collected for α-$Pb(N_3)_2$ at 0.0 GPa with an assessment of the quality of the fits obtained. Convergence was not attained during any refinement involving an angle restraint. Although the best fitting statistics were obtained during the refinement in which no restraints were applied, this resulted in chemically unreasonable bond distances and angles. The application of bond *and* length restraints did not have the desired effect of maintaining the linearity of the azide group and therefore were not performed for the higher-pressure data.

P (GPa)	*a* (Å)	*b* (Å)	*c* (Å)	*V* (Å^3)	wR_p
0.0	6.6363(13)	16.277(4)	11.3203(20)	1222.9(3)	0.046
0.32	6.6277(14)	16.265(5)	11.231(2)	1210.7(3)	0.058
0.66	6.6130(16)	16.248(5)	11.125(2)	1195.4(4)	0.075
0.99	6.6046(9)	16.241(3)	11.0464(13)	1184.9(2)	0.031
1.34	6.5943(20)	16.236(6)	10.946(3)	1171.9(5)	0.074
1.76	6.5894(20)	16.204(6)	10.874(3)	1161.0(5)	0.070
2.16	6.5755(10)	16.192(3)	10.7848(15)	1148.2(2)	0.034
2.38	6.5727(20)	16.185(6)	10.754(3)	1144.0(4)	0.083

Table 6.7 Unit cell parameters determined during compression of α-$Pb(N_3)_2$.

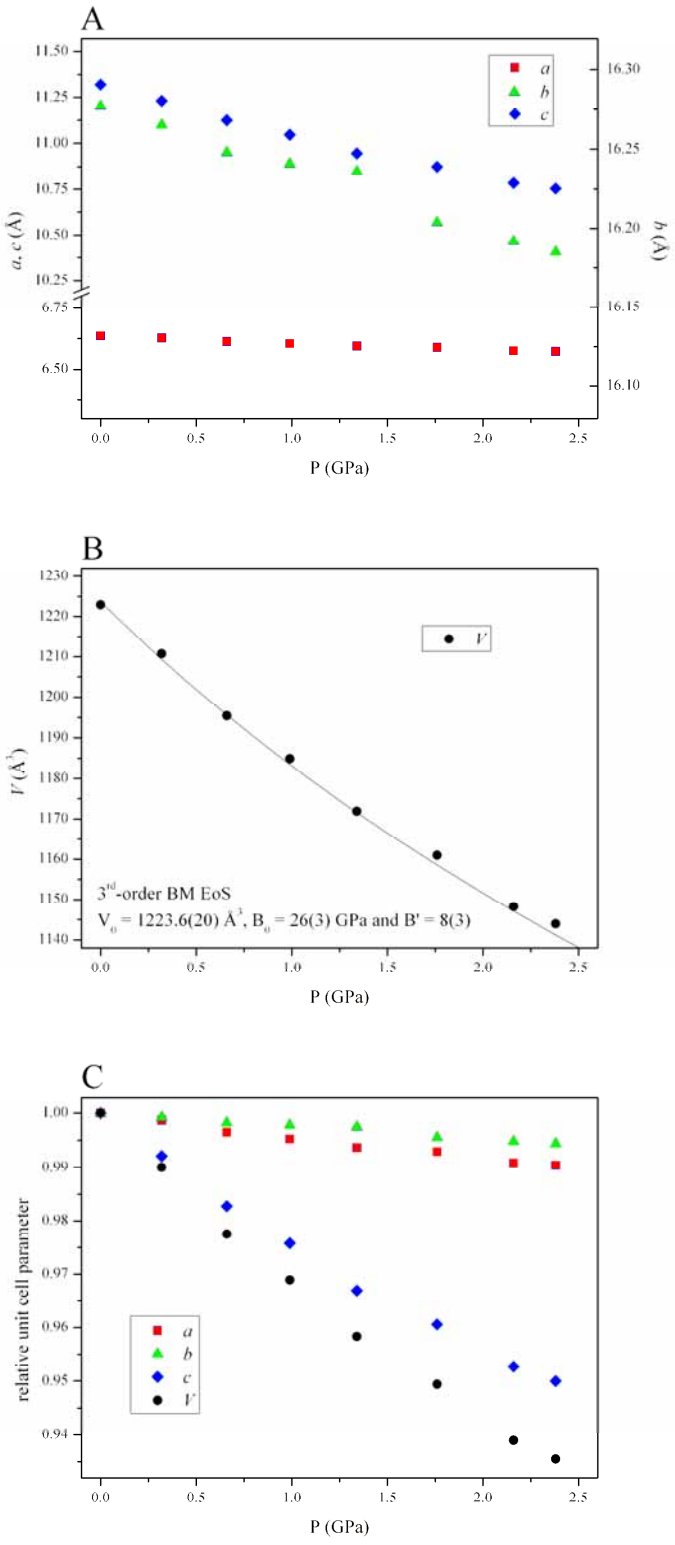

Figure 6.16 (a) Unit cell compression of α-$Pb(N_3)_2$; (b) Birch-Murnaghan *PV*-plot; and, (c) relative compression of the unit cell parameters, clearly showing the *c*-axis to be the most compressible.

While the structure remained chemically reasonable throughout, unfortunately no appreciable correlation between compression and structural parameters (such as the N-N and Pb…N distances, the N-N-N bond angles and the relative symmetry of each of the azides) was observed upon close inspection of the data. However, a plot of the relative contraction of the unit cell axes is illuminating (see Figure 6.16(c)). This clearly shows that the *c*-axis is considerably more compressible than either of the other axes, which is consistent with the relative thermal expansions of the axes at ambient pressure. This can be rationalised by noting that while one azide group aligns itself parallel to the *c*-axis, the other azides are completely perpendicular to this axis (Types I and III) or, in the case of Type II, almost perpendicular to it. This is shown in Figure 6.17. During compression the angle formed between a line drawn between the termini of Type II azides and the *c*-axis does gradually reduce, indicating that it is becoming more parallel with this axis, although this is still *ca* 25° at the upper pressure limit of the α-form.

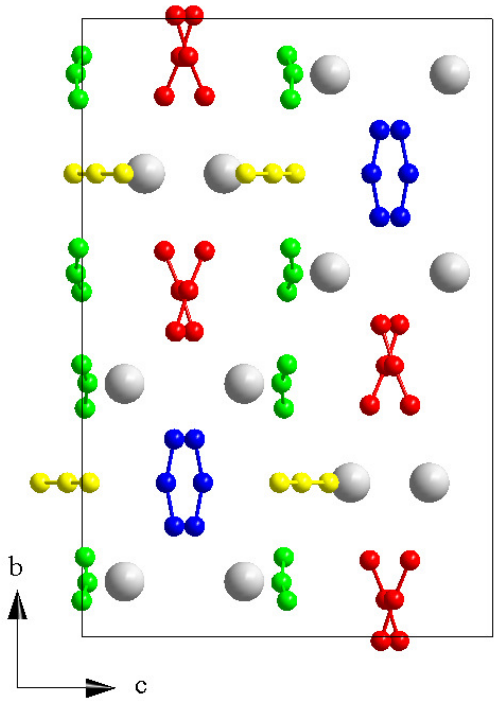

Figure 6.17 $Pb(N_3)_2$ viewed down the *a*-axis highlighting the orientation of the different azide groups. While three of the azide groups align themselves normal to the *c*-axis, only one (Type IV) is parallel to it.

The variation in the unit cell volume of α-$Pb(N_3)_2$ with increasing pressure has been fitted to a 3rd-order Birch-Murnaghan equation of state (EoS) with V_0 = 1223.6(20) Å^3, B_0 = 26(3) GPa and B' = 8(3). These values represent excellent agreement with our experimental result for V_0 (1222.9(3) Å^3) and the coefficients of the calculated Vinet EoS and F_E vs f_E plot. It is

also noteworthy that the bulk modulus for α-$Pb(N_3)_2$ is much closer to the bulk moduli reported for the ionic azides (NaN_3, CsN_3, TlN_3 and NH_4N_3) than that calculated for silver azide. This is despite both AgN_3 and $Pb(N_3)_2$ being regarded as co-ordinative azides, with a significant degree of covalency in their bonding. This observation may therefore suggest a more sophisticated classification of these compounds which accounts for their compression behaviour.

The observation of a new reflection in the diffraction pattern (at ~2.36 Å) with very little change in the rest of the diffraction pattern is clear evidence of a phase transition, most likely to a related structure. It is important to note that this peak is not coincident with any reflections in the neutron powder diffraction pattern calculated from the hexagonal ($P6_3/mmc$) structure of β-N_2 at 2.9 GPa.[50, 51] This, coupled with the observation that decompression to ambient pressure results in the recovery of the α-form, would suggest that this subtle change in the diffraction pattern is indicative of a phase transition to a new polymorph (ε-$Pb(N_3)_2$) rather than sample decomposition. Unfortunately the limited data range and the large unit cell volume have meant that it has so far been impossible to obtain an unambiguous indexing for this high-pressure polymorph. It would therefore be extremely useful to carry out complementary X-ray measurements, particularly on single crystals should they remain intact over this phase transition, to provide additional information. This would then allow Rietveld refinement of the neutron powder diffraction data collected in this study. This will provide extremely valuable information on the compression behaviour of ε-$Pb(N_3)_2$ to a maximum pressure of 5.8 GPa.

Summary: $Pb(N_3)_2$

The compression of α-$Pb(N_3)_2$ has been characterised by neutron powder diffraction and has been shown to manifest itself in the preferred contraction of the *c*-axis. Unfortunately the quality of the data obtained during this high-pressure experiment proved to be insufficient to allow one to make qualitative remarks about the inter- and intra-molecular interactions during compression, particularly the linearity and symmetry of the different azide groups. These data do, however, represent the first high-pressure study of this important energetic material. Furthermore, it is difficult to imagine a dramatic increase in data quality, especially within the time constraints of a typical neutron diffraction experiment; X-ray experiments may provide useful information (primarily unit cell parameters and Pb positions), but would be unlikely to aid in the refinement of the azide groups.

Another important result of this experiment has been the observation of another polymorph of lead(II) azide stable above 2.60 GPa, the structure of which has yet to be determined. This should therefore become a priority in the high-pressure study of these materials as this will aid in the understanding of the behaviour of $Pb(N_3)_2$ under operational conditions.

6.5 Summary and Conclusions

As in the more simple azides of sodium, caesium and thallium, the application of pressure has been particularly successful in inducing phase transitions in NH_4N_3, AgN_3 and $Pb(N_3)_2$. Each of these compounds has been found to adopt a new crystal structure at elevated pressure, although to date only γ-AgN_3 has been solved. These are significant observations, since polymorphic transitions may be expected to adversely affect the performance of these materials under detonation conditions. This is especially true for $Pb(N_3)_2$, which is still used extensively as a primary explosive. It is expected, therefore, that these studies will be of key importance to those who seek to improve the efficacy of predictive models of energetic performance (*i.e*. sensitivity, detonation velocity, *etc*). Moreover, the high-quality structural information will also be crucial for theoretical studies examining high-energy processes, such as the transition to detonation. The recent advances in the structural characterisation of these compounds have been reflected in an updated Table 6.8.

The ambient pressure structure of ND_4N_3 (α-form) has been observed to remain stable to 2.39 GPa. Up to this pressure, the compression is manifested in a rotation of half of the azide anions and an alignment of the tetrahedral cations. Further compression, however, results in a high-pressure phase transition at 2.6 GPa. Unfortunately, the structure solution of this β-form has been hampered by the limited range of *d*-spacing available and the relatively low resolution of the data obtained in these studies. Complementary X-ray powder and single-crystal diffraction studies are planned and it is expected that these experiments will be sufficient to elucidate the structure of β-NH_4N_3.

Interestingly, the compression of α-AgN_3 results in the removal of an orthorhombic distortion observed in the ambient-pressure structure – γ-AgN_3 adopts the archetypal tetragonal structure observed for CsN_3 and TlN_3 at under ambient conditions. Although this phase transition was predicted theoretically, the transition pressure was considerably higher than that observed experimentally. The most intriguing aspect of this study, however, was the slightly convex nature to the *PV*-plot obtained during compression of the γ-form. Such a feature, which suggests that the structure actually becomes more compressible at higher pressures, is unexpected, although previous observations of this behaviour have been

reported for network solids. Nevertheless, complementary high-pressure X-ray powder diffraction studies are suggested in order to confirm this result.

Finally, the high-pressure neutron diffraction study of lead(II) azide has been shown to yield a further polymorph, denoted ε-$Pb(N_3)_2$. Although subtle, the change in the diffraction patterns upon compression from 2.38 to 2.6 GPa is significant. It is therefore suggested that this transition involves a slight reduction in symmetry, or perhaps a monoclinic distortion of the orthorhombic unit cell. High-pressure X-ray powder diffraction studies would be beneficial in the structural characterisation of this ε-form by providing information on the unit cell parameters and heavy atom positions, thus complementing the neutron diffraction results presented herein.

6.6 Suggestions for Further Work

The primary focus of any high-pressure study of ammonium azide should be the collection of X-ray diffraction data. Although structure solution may be possible based on a combination of X-ray and neutron powder diffraction data, it is suggested that NH_4N_3 is a prime candidate for single-crystal compression studies. Provided single crystals are sufficiently stable at room temperature to allow their loading into a diamond-anvil cell, one would hope that refinement of single-crystal data would be straightforward. However, it should be noted that high-pressure phase transitions in the inorganic azides are often reconstructive in nature and it is currently not possible to predict whether single crystals would remain intact over the $\alpha \rightarrow \beta$ transition in NH_4N_3. Nevertheless, it would be interesting to conduct parallel studies on NH_4N_3 and ND_4N_3, since this will provide important information on the relative strengths of the hydrogen bonding interactions in these analogues, and whether deuteration results in any significant modifications to the compression behaviour of ammonium azide.

Further examination of the compression of silver azide by X-ray and neutron diffraction is also recommended, in order to corroborate the unusual compressibility curve observed in this work. Should this be the case, however, this clearly demonstrates the complexity of these systems and suggests that current theoretical models require some improvement. It would therefore be intriguing to conduct density functional theory (DFT) calculations with a view to re-creating the experimental compression behaviour. Furthermore, since the previous examples of structures with this anomalous compressibility also display negative thermal expansion at ambient pressure, a low temperature diffraction study is planned for AgN_3. Comparison of the material's thermal expansion at increasing pressure would be fascinating.

Finally, the high-pressure polymorph of lead(II) azide requires characterisation. Provided that the determination of the unit cell parameters is possible from future X-ray diffraction experiments, it is expected that structure solution may be viable on the basis of the neutron powder data collected in this work. A more complex undertaking may, in fact, be the crystallisation of the three other polymorphs that have been observed at ambient pressure (β, γ and δ). It would be particularly pleasing to solve the structure of the triclinic δ-form, as this represents a significant departure from the structures of many of the other azides in this study, the majority of which adopt orthorhombic symmetry or higher.

Polymorph	Space Group	*a* (Å)	*b* (Å)	*c* (Å)	*α* (°)	*β* (°)	*γ* (°)	Atomic positions?	*P*/*T* conditions	Ref.
α-NH_4N_3	*Pmna*	8.948(3)	3.808(2)	8.659(3)	90	90	90	Yes	Ambient *P*/*T*	[3]
β-NH_4N_3	-	-	-	-	-	-	-	-	***P* > 2.6 GPa; Ambient *T***	**this study**
α-AgN_3	*Ibam*	5.600(1)	5.980(6)	5.998(1)	90	90	90	Yes	Ambient *P*; *T* < 443 K	[11]
β-AgN_3	$P2_1/c$	6.0756(2)	6.1663(2)	6.5729(2)	90	114.19(0)	90	Yes	Ambient *P*; *T* > 443 K Recovered to ambient *P*/*T*	[16]
γ-AgN_3	***I4/mcm***	**5.7239(11)**	**5.7239(11)**	**5.9338(14)**	**90**	**90**	**90**	**Yes**	***P* > 0.80 GPa; Ambient *T***	**this study**
α-$Pb(N_3)_2$	*Pnma*	6.63	16.25	11.31	90	90	90	Yes	Ambient *P*/*T*	[24],[28]
β-$Pb(N_3)_2$	-	18.31	8.88	5.12	90	107.5	90	No	Ambient *P*/*T*	[22]
γ-$Pb(N_3)_2$	-	12.060	10.507	6.505	90	95.75	90	No	Ambient *P*/*T*; low pH/additives	[20]
δ-$Pb(N_3)_2$	-	13.163	10.532	6.531	90.53	98.12	112.67	No	Ambient *P*/*T*; low pH/additives	[20]
ε-$Pb(N_3)_2$	-	-	-	-	-	-	-	-	***P* > 2.6 GPa; Ambient *T***	**this study**

Table 6.8 Structural data for ammonium, silver and lead(II) azides at variable temperature and pressure. The results of the current study (bold) have been included alongside previous reports.

6.7 References

1. L.K. Frevel, *Z. Kristallogr.*, 1936, **94**, 197.
2. T.C. Waddington, *J. Chem. Soc.*, 1958, 4340.
3. E. Prince and C.S. Choi, *Acta Cryst.*, 1978, **B34**, 2606.
4. H.S. de Amorim, M.R. do Amaral Jr., P. Pattison, I.P. Ludka, and J.C. Mendes, *Rev. Soc. Quim. Mex.*, 2002, **4**, 313.
5. O. Reckeweg and A. Simon, *Z. Naturforsch.*, 2003, **58**, 1097.
6. D.A. Dows, E. Whittle, and G.C. Pimentel, *J. Chem. Phys.*, 1955, **23**, 1475.
7. W.L. Ng and J.E. Field, *Thermochim. Acta*, 1985, **84**, 133.
8. U. Müller, *Strukturchemie der Azide*, in *Structure and Bonding, Inorganic Chemistry, Vol. 14*, 1973, Springer, Berlin/Heidelberg.
9. T.C. Waddington, *J. Chem. Soc*, 1959, 2499.
10. H.E. Marr, III and R.H. Stanford, Jnr, *Acta Cryst.*, 1962, **15**, 1313.
11. G.C. Guo, Q.M. Wang, and T.C.W. Mak, *J. Chem. Crystallogr.*, 1999, **29**, 561.
12. C.D. West, *Z. Kristallogr.*, 1936, **95**, 421.
13. J.I. Bryant and R.L. Brooks, *J. Chem. Phys.*, 1971, **54**, 5315.
14. K. Dehnicke, *Z. Anorg. Allg. Chem.*, 1974, **409**, 311.
15. C.M. Pereira and M.M. Chaudhri, 1988, **57**, 173
16. C.L. Schmidt, R. Dinnebier, U. Wedig, and M. Jansen, *Inorg. Chem.*, 2007, **46**.
17. G.M. Diamant, A.E. Saprykin, and Y.Y. Sidorin, *Reactivity of Solids*, 1989, **7**, 375.
18. C.M. Pereira and M.M. Chaudhri, *J. Energetic Mater.*, 1989, **7**, 297
19. W. Zhu and H. Xiao, *J. Solid State Chem.*, 2007, **180**, 3521.
20. S. Lamnevik and R. Söderquist, *FOA Report A 1174 - F110*, 1964.
21. F.D. Miles, *J. Chem. Soc.*, 1931, 2532.
22. K. Hattori and W. McCrone, *Anal. Chem.*, 1956, **28**, 1792.
23. G.W.C. Taylor and A.T. Thomas, *J. Cryst. Growth*, 1968, **3-4**, 391.
24. L.V. Azaroff, *Z. Kristallogr.*, 1956, **107**, 362.
25. K. Hattori and W. McCrone, *Anal. Chem.*, 1956, **28**, 1791.
26. C.S. Choi and H.P. Boutin, *Acta Cryst.*, 1969, **B25**, 982.
27. G.L. Glen, *J Am. Chem. Soc.*, 1963, **85**, 3892.
28. C.S. Choi, E. Prince, and W.L. Garrett, *Acta Cryst.*, 1977, **B33**, 3536.
29. Z. Iqbal, W. Garrett, C.W. Brown, and S.S. Mitra, *J. Chem. Phys.*, 1971, **55**, 4528.
30. W. Zhu and H. Xiao, *J. Phys. Chem. B*, 2006, **110**, 18196.
31. F.A. Mauer, C.R. Hubbard, and T.A. Hahn, *J. Chem. Phys.*, 1974, **60**, 1341.
32. C.E. Weir, S. Block, and G.J. Piermarini, *J. Chem. Phys.*, 1970, **53**, 4265.
33. W.F. Perger, *Int. J. Quantum Chem.*, 2010, **110**, 1916.
34. T.A. Richter, *Synthesis and Chemical Properties*, in *Energetic Materials 1: Physics and Chemistry of the Inorganic Azides*, H.D. Fair and R.F. Walker, Editors, 1977, Plenum Press, New York.
35. W.G. Marshall and D.J. Francis, *J. Appl. Crystallogr.*, 2002, **35**, 122.
36. A.D. Fortes, PhD Thesis, 2004, Department of Earth Sciences, University College, London, UK.
37. J.M. Besson, R.J. Nelmes, G. Hamel, J.S. Loveday, G. Weill, and S. Hull, *Physica B*, 1992, **180-181**, 907.
38. R. Von Dreele and A.C. Larson, *General Structure Analysis System (GSAS)*, 1986.
39. R.J. Angel, *Equations of State*, in *Reviews in Mineralogy and Geochemistry, 41: High-Temperature and High-Pressure Crystal Chemistry*, R.M. Hazen and R.T. Downs, Editors, 2000, Mineralogical Society of America, Washington, D.C., USA.
40. K.W. Chapman and P.J. Chupas, *J. Am. Chem. Soc.*, 2007, **129**, 10090.
41. K.W. Chapman, G.J. Halder, and P.J. Chupas, *J. Am. Chem. Soc.*, 2009, **131**, 17546.
42. P. Vinet, J. Ferrante, J.R. Smith, and J.H. Rose, *J. Phys. C: Solid State Phys.*, 1986, **19**, L467.

43. S.E. Sheppard and W. Vanselow, *J. Phys. Chem.*, 1929, **33**, 250.
44. J.P. Abid, A.W. Wark, P.F. Brevet, and H.H. Girault, *Chem. Commun.*, 2002, **38**, 792.
45. O.V. Mikhailov, A.V. Kondakov, and R.I. Krikunenko, *High Energy Chem.*, 2005, **39**, 324.
46. L. Wohler, *Chem. Ztg*, 1912, **35**, 1096.
47. E.P. Surovoi, S.M. Sirik, Y.A. Zakharov, L.N. Bugerko, and I.K. Kilina, *Zhurnal Nauchnoi i Prikladnoi Fotografii*, 2000, **45**, 14.
48. E.P. Surovoi, S.M. Sirik, and L.N. Bugerko, *Materialovedenie*, 2008, **5**, 40.
49. R. Von Dreele, *personal communication*, 2010.
50. D. Schiferl, D.T. Cromer, R.R. Ryan, A.C. Larson, R. LeSar, and R.L. Mills, *Acta Cryst.*, 1983, **C39**, 1151.
51. J. Belak, R. LeSar, and R.D. Etters, *J. Chem. Phys.*, 1990, **92**, 5430.

Chapter 7

General Remarks

7 General Remarks

This study highlights the importance of obtaining high-quality structural information on energetic materials over a range of temperatures and pressures. The high-pressure/high-temperature polymorph of RDX has been determined and has been shown to be distinct from the highly metastable β-form at ambient conditions, with which is it has previously been confused. This has led to it being re-named the ε-form. Furthermore, an equation of state has been obtained for RDX up to a maximum pressure of 23 GPa. At no point during this study was a transition to δ-RDX observed, contrary to previous spectroscopic results.

The high-pressure behaviour of another high explosive, CL-20, has also been investigated. It was found that compression of ε-CL-20 (the most thermodynamically stable form at ambient conditions) to 7.2 GPa, did not result in any polymorphic transitions. The γ-form, however, was found to be more susceptible to pressure-induced phase transitions and, moreover, the nature of these transitions depended upon the pressure-transmitting medium used. For example, compression of γ-CL-20 in Fluorinert produced the ζ polymorph, while compression in MeOH:EtOH resulted in pressure-induced solvate formation.

Finally, a series of metal azides (NaN_3, CsN_3, TlN_3, NH_4N_3, AgN_3 and $Pb(N_3)_2$) have been shown to display remarkable polymorphism at variable temperatures and pressures. All have been observed to undergo at least one phase transition, and a total of 10 new polymorphs have been identified.

The number of high-pressure polymorphs identified in this work is a reflection, not only of the powerful role that pressure plays in dramatically altering the relative energies of different crystal structures, but also the technical advances which have facilitated the collection and refinement of complementary high-pressure structural data. Furthermore, the success of these studies highlights the unrivalled opportunity for obtaining novel materials that high-pressure studies provide and the exciting prospect of the recovery of high-pressure phases to ambient conditions. This has been proposed as an effective way of improving performance of energetic materials (such as crystal density, reduced sensitivity, etc) without the need for changing their molecular structure.

It would therefore be advised to extend these studies to other energetic materials, in the first instance HMX, FOX-7 and octanitrocubane. Indeed high-pressure techniques may provide a viable route to the denser form of octanitrocubane that has been predicted theoretically (see Section 1.2.2). Should this be the case, recovery of this form to ambient conditions would be a remarkable achievement and would emphasise the importance of such experiments to the

energetics community. An alternative approach to the structural modification of energetic materials is to co-crystallise them with simple organic molecules, with a view to tailoring their detonation characteristics, particularly sensitivity. Although not actively explored in this research, it has been observed that the crystal structure of CL-20 is sufficiently porous to allow the formation of a 2:1 CL-20:MeOH solvate at pressure, which is recoverable to ambient conditions. Thus the possibility of obtaining co-crystals of CL-20, HMX and various other energetic materials should be explored.

Naturally, the performance characteristics of recovered high-pressure forms and co-crystals will need to be rigorously assessed. It will therefore be necessary to collaborate with defence scientists who have experience conducting sensitivity studies. Other collaborative projects may involve theoreticians and shock physicists. It is anticipated that the experimental data presented in this work will complement theoretical studies focussed on the predictive modelling of energetic performance, particularly detonation velocities and sensitivities. In a more general sense, however, these high-pressure studies will also prove to be excellent candidates to test the validity of intermolecular potentials used to describe these materials. Meanwhile, the spectroscopic identification of new high-pressure polymorphs may be possible at the very high pressures attainable in shock compression studies, although their structural solution is far more problematic. The results of these experiments, however, may guide diffraction studies like those conducted in the present work.

Finally, it is also hoped that the rich polymorphism of the metal azides (NaN_3, CsN_3, TlN_3, NH_4N_3, AgN_3 and $Pb(N_3)_2$) at extreme conditions will lead to the extension of this study to include other metal azides (such as KN_3, RbN_3) as well as analogous binary systems, for example metal bifluorides (MHF_2), cyanates (MOCN) and thiocyanates (MSCN).

In addition, the photolysis of CsN_3 to produce Cs metal and, potentially, polynitrogen species has opened up a further avenue for the application of high-pressure techniques in the synthesis of ‘high-energy density materials’. In the immediate future the identification of the optimum conditions for photolysis and the characterisation of the photolysis products are advised. However, it is anticipated that these studies may then be extended to more complex azides containing a greater proportion of nitrogen, for example $[Cr(III)(N_3)_6]^{3-}$. Of course rigorous studies will have to be completed on the synthesis of such complexes, their structures and their reactivities. Furthermore, detailed investigations of the product species must also be conducted before their application in munitions.

Appendix

Crystallographic Information

Conferences and Lecture Course Attended

Publications

8 Appendix

8.1 Crystallographic Information

8.1.1 Chapter 3

X-ray Single Crystal Data	**β-RDX at 273 K**
Crystal Data	
Chemical Formula	C3 H6 N6 O6
M_r	222.12
Cell setting, space group	Orthorhombic, $Pca2_1$
Temperature (K)	273
a, b, c (Å)	15.0972(7), 7.5463(4), 14.4316(6)
V (Å^3)	1644.16(13)
Z	8
D_c (Mg m^{-3})	1.795
Radiation type	Mo-Kα
No. reflections for cell parameters	2672
θ range (°)	3-23
μ (mm^{-1})	0.171
Crystal form, colour	Lathe, colourless
Crystal size (mm)	0.05 x 0.20 x 0.45
Data Collection	
Diffractometer	Bruker SMART
Data collection method	ω
Absorption correction	Multiscan
T_{min}	0.67
T_{max}	0.97
No. of measured, independent and observed reflections	10137, 1244
Criterion for observed reflections	$I > 2.00u(I)$
R_{int}	0.055
θ_{max} (°)	23.312
Range of h, k, l	-16 → h → 16 -8 → k → 8 -16 → l → 15
Refinement	
Refinement on	F^2
$R[F^2 > 2\sigma(F^2)]$, $wR(F^2)$, S	0.0975, 0.1405, 0.7647
No. of reflections	1244
No. of parameters	271
H-atom treatment	Constrained to parent
Weighting scheme	Calculated $w = 1/[\sigma^2(F^2) + (0.08P)^2 + 0.56P]$ where $P = (\max(F_o^2,0) + 2F_c^2)/3$
(Δ/σ)max	0.000045
$\Delta\rho_{max}$, $\Delta\rho_{min}$ (e Å^{-3})	0.52, -0.43

X-ray Single Crystal Data	β-RDX at 150 K
Crystal Data	
Chemical Formula	C3 H6 N6 O6
M_r	222.12
Cell setting, space group	Orthorhombic, $Pca2_1$
Temperature (K)	150
a, b, c (Å)	15.1267(11), 7.4563(6), 14.3719(11)
V (Å^3)	1621.0(2)
Z	8
D_c (Mg m^{-3})	1.820
Radiation type	Mo-Kα
No. reflections for cell parameters	2888
θ range (°)	3-24
μ (mm^{-1})	0.0173
Crystal form, colour	Block, colourless
Crystal size (mm)	0.15 x 0.23 x 0.38
Data Collection	
Diffractometer	Bruker SMART
Data collection method	ω
Absorption correction	Multiscan
T_{min}	0.85
T_{max}	0.97
No. of measured, independent and observed reflections	10899, 2097
Criterion for observed reflections	$I > 2.00u(I)$
R_{int}	0.038
θ_{max} (°)	28.425
Range of h, k, l	-20 → h → 14 -8 → k → 9 -19 → l → 14
Refinement	
Refinement on	F^2
$R[F^2 > 2\sigma(F^2)]$, $wR(F^2)$, S	0.0465, 0.0847, 0.8136
No. of reflections	2097
No. of parameters	271
H-atom treatment	Constrained to parent
Weighting scheme	Calculated $w = 1/[\sigma^2(F^2) + (0.03P)^2 + 0.00P]$ where $P = (\max(F_o^2,0) + 2F_c^2)/3$
(Δ/σ)max	0.000149
$\Delta\rho_{max}$, $\Delta\rho_{min}$ (e Å^{-3})	0.48, -0.34

X-ray Single Crystal Data	ε-RDX at 293(2) K, 5.70(5) GPa
Crystal Data	
Chemical Formula	C3 H6 N6 O6
M_r	222.12
Cell setting, space group	Orthorhombic, $Pca2_1$
Temperature (K)	293(2)
a, b, c (Å)	7.0324(11), 10.530(3), 8.7909(11)
V (Å^3)	651.0(2)
Z	8
D_c (Mg m^{-3})	2.266
Radiation type	Mo-Kα
No. reflections for cell parameters	430
θ range (°)	3-19
μ (mm^{-1})	0.216
Crystal form, colour	Block, colourless
Crystal size (mm)	0.05 x 0.05 x 0.10
Data Collection	
Diffractometer	Bruker Nonius APEX II
Data collection method	ω
Absorption correction	Multiscan
T_{min}	0.86
T_{max}	0.99
No. of measured, independent and observed reflections	3740, 333
Criterion for observed reflections	$I > 2.00u(I)$
R_{int}	0.0916
θ_{max} (°)	26.910
Range of h, k, l	$-8 \rightarrow h \rightarrow 8$ $-6 \rightarrow k \rightarrow 5$ $-11 \rightarrow l \rightarrow 10$
Refinement	
Refinement on	F^2
$R[F^2 > 2\sigma(F^2)]$, $wR(F^2)$, S	0.0578, 0.1102, 1.0337
No. of reflections	333
No. of parameters	61
H-atom treatment	Constrained to parent
Weighting scheme	Calculated $w = 1/[\sigma^2(F^2) + (0.06P)^2 + 0.92P]$ where $P = (\max(F_o^2,0) + 2F_c^2)/3$
(Δ/σ)max	0.000051
$\Delta\rho_{max}$, $\Delta\rho_{min}$ (e Å^{-3})	0.44, -0.47

8.1.2 Chapter 4

X-ray Single Crystal Data	**ζ-CL-20 at 293(2) K, 3.30(5) GPa**
Crystal Data	
Chemical Formula	C6 H6 N12 O12
M_r	438.19
Cell setting, space group	Monoclinic, $P2_1/n$
Temperature (K)	293(2)
a, b, c (Å)	12.579(2), 7.7219(19), 14.1260(15)
β (°)	111.218(10)
V (Å^3)	1279.1(4)
Z	4
D_c (Mg m^{-3})	2.275
Radiation type	Mo-Kα
No. reflections for cell parameters	676
θ range (°)	3-22
μ (mm^{-1})	0.218
Crystal form, colour	Block, colourless
Crystal size (mm)	0.05 x 0.05 x 0.10
Data Collection	
Diffractometer	Bruker Nonius APEX II
Data collection method	ω
Absorption correction	Multiscan
T_{min}	0.99
T_{max}	0.99
No. of measured, independent and observed reflections	5107, 935
Criterion for observed reflections	$I > 2.00u(I)$
R_{int}	0.128
θ_{max} (°)	23.345
Range of h, k, l	-13 → h → 13 -5 → k → 5 -15 → l → 15
Refinement	
Refinement on	F
$R[F^2 > 2\sigma(F^2)]$, $wR(F^2)$, S	0.0877, 0.0885, 1.1244
No. of reflections	515
No. of parameters	121
H-atom treatment	Constrained to parent
Weighting scheme	Calculated $w = 1.0/[A_0T_0(x) + A_1T_1(x) + A_{n-1}T_{n-1}(x)]$, where A_i are the Chebychev coefficients (A_i = 1.17, 0.787, 0.789) and $x = F_{calc}/F_{max}$
(Δ/σ)max	0.0000906
$\Delta\rho_{max}$, $\Delta\rho_{min}$ (e Å^{-3})	-0.54, 0.48

X-ray Single Crystal Data	CL-20:MeOH (2:1) solvate at 100 K
Crystal Data	
Chemical Formula	2(C6 H6 N12 O12): (CO)
M_r	448.19
Cell setting, space group	Orthorhombic, *Pbca*
Temperature (K)	100
a, b, c (Å)	9.6445(5), 13.2186(7), 23.3407(8)
V (Å^3)	2975.6(2)
Z	8
D_c (Mg m^{-3})	2.001
Radiation type	Cu-Kα
No. reflections for cell parameters	6542
θ range (°)	2-73
μ (mm^{-1})	5.097
Crystal form, colour	Block, colourless
Crystal size (mm)	0.0722 x 0.0918 x 0.2600
Data Collection	
Diffractometer	OD Supernova
Data collection method	ω
Absorption correction	Multiscan
T_{min}	0.52533
T_{max}	1.00000
No. of measured, independent and observed reflections	16053, 2920
Criterion for observed reflections	$I > 2.00u(I)$
R_{int}	0.066
θ_{max} (°)	73.212
Range of h, k, l	-11 → h → 11 -16 → k → 11 -28 → l → 28
Refinement	
Refinement on	F^2
$R[F^2 > 2\sigma(F^2)]$, $wR(F^2)$, S	0.0756, 0.1991, 0.9563
No. of reflections	2920
No. of parameters	286
H-atom treatment	Constrained to parent
Weighting scheme	Calculated $w = 1/[\sigma^2(F^2) + (0.12P)^2 + 9.25P]$ where $P = (\max(F_o^2,0) + 2F_c^2)/3$
(Δ/σ)max	0.0000915
$\Delta\rho_{max}$, $\Delta\rho_{min}$ (e Å^{-3})	0.79, -0.47

8.2 Quality of Fit: Equations of State

Polymorph	Model	Coefficients	Fitting Statistics*
ε-RDX-d_6	Murnaghan	V_0 = 808(4) Å^3 B_0 = 10.3(8) GPa B' = 7.8(3)	R_u = 1.179% χ^2_u = 0.0019 R_w = 1.469% χ^2_w = 0.7676
γ-RDX-h_6 (MeOH:EtOH)	3rd-order Birch-Murnaghan	V_0 = 1632 Å^3 (fixed) B_0 = 14(3) GPa B' = 8.4(18)	R_u = 5.597% χ^2_u = 0.8619 R_w = 6.238% χ^2_w = 0.8532
γ-RDX-h_6 (no medium)	3rd-order Birch-Murnaghan	V_0 = 1632 Å^3 (fixed) B_0 = 11(6) GPa B' = 8(4)	R_u = 2.887% χ^2_u = 0.4630 R_w = 3.468% χ^2_w = 0.4526
ε-CL-20	3rd-order Birch-Murnaghan	V_0 = 1431.8 Å^3 (fixed) B_0 = 9.5(22) GPa B' = 27(8)	R_u = 5.542% χ^2_u = 0.0877 R_w = 5.888% χ^2_w = 11.9400
CL-20:MeOH (2:1)	3rd-order Birch-Murnaghan	V_0 = 3120.6 Å^3 (fixed) B_0 = 4.6(5) GPa B' = 27(4)	R_u = 1.092% χ^2_u = 0.0017 R_w = 1.156% χ^2_w = 0.6292
	Vinet	V_0 = 3120.6 Å^3 (fixed) B_0 = 6.6(5) GPa B' = 13.6(8)	R_u = 2.068% χ^2_u = 0.0039 R_w = 1.995% χ^2_w = 0.0039
	3rd-order Birch-Murnaghan (P_{offset} = 0.57 GPa)	V_0 = 2922.0 Å^3 (fixed) B_0 = 17.2(10) GPa B' = 10.1(12)	R_u = 0.394% χ^2_u = 0.0001 R_w = 0.366% χ^2_w = 0.0458
	Vinet (P_{offset} = 0.57 GPa)	V_0 = 2922.0 Å^3 B_0 = 17.5(8) GPa B' = 9.2(8)	R_u = 0.353% χ^2_u = 0.0001 R_w = 0.337% χ^2_w = 0.0043
α-NaN_3	3rd-order Birch-Murnaghan	V_0 = 116.9(2) Å^3 B_0 = 15.1(7) GPa B' = 7.0(5)	R_u = 1.366% χ^2_u = 0.0028 R_w = 1.489% χ^2_w = 1.1315
CsN_3-III	3rd-order Birch-Murnaghan (P_{offset} 0.54 GPa)	V_0 = 325.98 Å^3 (fixed) B_0 = 19.7(10) GPa B' = 5.8(11)	R_u = 1.358% χ^2_u = 0.0007 R_w = 1.377% χ^2_w = 0.2862
TlN_3-II	2nd-order Birch-Murnaghan	V_0 = 283.0(9) Å^3 B_0 = 21(3) GPa B' = 4 (fixed)	R_u = 4.404% χ^2_u = 0.0008 R_w = 4.508% χ^2_w = 0.3015
TlN_3-III	3rd-order Birch-Murnaghan (P_{offset} = 0.76 GPa)	V_0 = 267.14 Å^3 (fixed) B_0 = 24.1(5) GPa B' = 6.7(4)	R_u = 0.566% χ^2_u = 0.0005 R_w = 0.574% χ^2_w = 0.1827
α-ND_4N_3	2nd-order Birch-Murnaghan	V_0 = 295.7(4) Å^3 B_0 = 20.2(5) GPa B' = 4 (fixed)	R_u = 2.813% χ^2_u = 0.0022 R_w = 2.876% χ^2_w = 0.8566
γ-AgN_3	3rd-order Birch-Murnaghan	V_0 = 200.86 Å^3 (fixed) B_0 = 26.2(25) GPa B' = 17(4)	R_u = 3.901% χ^2_u = 0.0251 R_w = 4.735% χ^2_w = 7.4663
	Vinet	V_0 = 200.86 Å^3 (fixed) B_0 = 27.9(21) GPa B' = 13.2(19)	R_u = 3.987% χ^2_u = 0.0273 R_w = 4.968% χ^2_w = 8.2143
	3rd-order Birch-Murnaghan	V_0 = 197.2(4) Å^3 B_0 = 60(5) GPa B' = 1.3(15)	R_u = 1.918% χ^2_u = 0.0063 R_w = 2.187% χ^2_w = 1.9145

Polymorph	Model	Coefficients	Fitting Statistics*
γ-AgN_3 (contd)	Vinet	V_0 = 197.2(4) Å^3 B_0 = 60(6) GPa B' = 0.9(20)	R_u = 1.925% χ^2_u = 0.0063 R_w = 2.185% χ^2_w = 1.9134
	3rd-order Birch-Murnaghan (P_{offset} = 0.80 GPa)	V_0 = 194.14 Å^3 (fixed) B_0 = 70(3) GPa B' = -1.4(14)	R_u = 3.601% χ^2_u = 0.0125 R_w = 4.118% χ^2_w = 3.6983
	Vinet (P_{offset} = 0.80 GPa)	V_0 = 194.14 Å^3 (fixed) B_0 = 71(4) GPa B' = -2.5(19)	R_u = 3.566% χ^2_u = 0.0122 R_w = 4.072% χ^2_w = 3.6114
α-$Pb(N_3)_2$	3rd-order Birch-Murnaghan	V_0 = 1223.6(20) Å^3 B_0 = 26(3) GPa B' = 8(3)	R_u = 2.029% χ^2_u = 0.0006 R_w = 1.741% χ^2_w = 0.0006

* Fitting statistics obtained from EoSFIT output file.

8.3 Conferences and Lecture Courses Attended

8.3.1 Year 1

Oral Presentation

David I.A. Millar, Adam S. Cumming, Duncan J. Francis, William G. Marshall, Iain D.H. Oswald and Colin R. Pulham, **High-Pressure Structural Studies of Energetic Materials**, *Neutron and Muon User Meeting: Young Scientist Talks*, Nottingham, UK, March 2008.

Poster Presentations

David I.A. Millar, Adam S. Cumming, Duncan J. Francis, William G. Marshall, Iain D.H. Oswald and Colin R. Pulham, **High-Pressure Structural Studies of Energetic Materials**, *British Crystallographic Association: Spring Meeting*, York, UK, April 2008.

David I.A. Millar, Adam S. Cumming, Duncan J. Francis, William G. Marshall, Iain D.H. Oswald and Colin R. Pulham, **High-Pressure Structural Studies of Energetic Materials**, *Gordon Research Conference: Energetic Materials*, Tilton, NH, USA, June 2008.

David I.A. Millar, Adam S. Cumming, Duncan J. Francis, William G. Marshall, Iain D.H. Oswald and Colin R. Pulham, **The Crystal Structure of β-RDX: An Elusive Form of an Explosive Revealed**, *ISIS Crystallography Group: User Meeting*, Abingdon, Oxon., UK, November 2008.

Courses Attended

EaStCHEM: Academic Paper Writing, St Andrews, UK, April 2008.

Scottish Universities Summer School in Physics (Number 63): High-Pressure Physics, Skye, UK, May 2008.

8.3.2 Year 2

Oral Presentation

David I.A. Millar, Adam S. Cumming, Duncan J. Francis, William G. Marshall, Iain D.H. Oswald and Colin R. Pulham, **Pressure-Cooking Explosives: A Tale of Two Polymorphs**, *British Crystallographic Association: Young Crystallographers' Satellite Meeting*, Loughborough, UK, April 2009.

Poster Presentations

David I.A. Millar, Adam S. Cumming, Duncan J. Francis, William G. Marshall, Iain D.H. Oswald and Colin R. Pulham, **Pressure-Cooking Explosives: A Tale of Two Polymorphs**, *British Crystallographic Association: Spring Meeting*, Loughborough, UK, April 2009.

Courses Attended

12th BCA/CCG Intensive Training School in X-ray Structure Analysis, Durham, UK, April 2009.

41st Course on High-Pressure Crystallography: From Novel Experimental Approaches to Applications in Cutting-Edge Technologies, Erice, Italy, June 2009.

DLS Workshop: Defects in Structural Materials, Didcot, UK, September 2009.

Transkills: Introduction to UNIX, Edinburgh, UK, November 2009.

8.3.3 Year 3

Oral Presentation

David I.A. Millar, Christopher Barry, Adam S. Cumming, Duncan J. Francis, Annette K. Kleppe, William G. Marshall, Helen E. Maynard-Casely, Iain D.H. Oswald and Colin R. Pulham, **Energetic Materials at Extreme Conditions: RDX and CL-20**, *Edinburgh Postgraduate Seminar*, May 2010.

Poster Presentation

David I.A. Millar, Adam S. Cumming, Craig A. Henderson, Anna Muszkiewicz and Colin R. Pulham, **Co-Crystallisation of Energetic Materials: A Step Towards Tailored**

Munitions, *British Crystallographic Association: Spring Meeting*, Warwick, April 2010. **[Awarded International Centre for Diffraction Data (ICDD) Bursary]**

David I.A. Millar, Christopher Barry, Adam S. Cumming, Duncan J. Francis, Annette K. Kleppe, William G. Marshall, Helen E. Maynard-Casely, Iain D.H. Oswald and Colin R. Pulham, **Energetic Materials at Extreme Conditions: The Power of Pressure**, *Gordon Research Conference: Energetic Materials*, Tilton, NH, USA, June 2010.

Courses Attended

Transkills: Publishing with LaTeX, Edinburgh, UK, December 2009.

8.4 Publications

Alistair J. Davidson, Iain D.H. Oswald, Duncan J. Francis, Alistair R. Lennie, William G. Marshall, David I.A. Millar, Colin R. Pulham, John E. Warren and Adam S. Cumming, **Explosives under pressure – the crystal structure of γ-RDX as determined by high-pressure X-ray and neutron diffraction**, *CrystEngComm*, 2008, **10**(2), 162-165. **[Highlighted in *Chemical Science*, December 2007]**

David I.A. Millar, Iain D.H. Oswald, Duncan J. Francis, William G. Marshall, Colin R. Pulham and Adam S. Cumming, **The crystal structure of β-RDX – an elusive form of an explosive revealed**, *Chem. Commun*., 2009, **45**(5), 562-564.

David I.A. Millar, William G. Marshall, Iain D.H. Oswald and Colin R. Pulham, **High-pressure structural studies of energetic materials**, *Crystallogr. Rev*., 2010, **16**(2), 115-132.

David I.A. Millar, Helen E. Maynard-Casely, Annette K. Kleppe, William G. Marshall, Colin R. Pulham and Adam S. Cumming, **Putting the squeeze on energetic materials – structural characterisation of a high-pressure phase of CL-20**, *CrystEngComm*, 2010, **12**, 2524-2527.

David I.A. Millar, Iain D.H. Oswald, Christopher Barry, Duncan J. Francis, William G. Marshall, Colin R. Pulham and Adam S. Cumming, **Pressure-cooking explosives – the crystal structure of ε-RDX as determined by X-ray and neutron diffraction**, *Chem. Commun.*, 2010, **46**(31), 5662-5664. **[Hot Article]**